Scan-by-Scan Storm-Motion Deviations for Concurrent Tornadic and Nontornadic Supercells

MATTHEW J. BUNKERS,[a] MATTHEW B. WILSON,[b] MATTHEW S. VAN DEN BROEKE,[b] AND DEVON J. HEALEY[b]

[a] *NOAA/National Weather Service, Rapid City, South Dakota*
[b] *University of Nebraska–Lincoln, Lincoln, Nebraska*

(Manuscript received 19 September 2021, in final form 28 February 2022)

ABSTRACT: In this exploratory study, storm-motion deviations are examined for concurrent tornadic and nontornadic supercells using 171 cases. This deviation, or "delta," is defined as the shear-orthogonal distance between the observed supercell motion and a baseline supercell-motion prediction. Larger deltas—representing supercells moving farther right (in a shear-relative sense) compared to the baseline prediction—are hypothesized as more likely to be associated with tornadoes than nearby supercells with smaller deltas, consistent with recent research. Automated radar tracking is used to calculate supercell motion every scan, which then is compared to a model-derived hourly supercell-motion prediction to calculate the deltas. Tornadic supercells have larger average deltas (by 1.9–2.0 m s^{-1}) than nearby nontornadic supercells when using 20- and 30-min storm-motion calculations, and the deltas are larger for the tornadic versus nontornadic supercells ~80% of the time. Average delta trends also are positive 62%–70% of the time prior to tornadogenesis. The supercell-motion deltas show a modest positive correlation with EF-scale damage rating, indicating a possible relationship between tornado rating and storm deviation. The relative delta differences between tornadic and nontornadic supercells appear more meaningful than the absolute delta magnitudes (i.e., about 70% of tornadic cases with negative average deltas had deltas that were less negative compared to concurrent nontornadic supercells). This concept shows promise as a potential tool to assist operational forecasters in tornado warning decisions.

SIGNIFICANCE STATEMENT: Supercells are rotating thunderstorms, and these storms produce the most destructive tornadoes. However, it has been challenging to forecast which supercells will produce tornadoes. In this exploratory study to help better forecast supercell tornadoes, we looked at how the observed supercell motion compared to the predicted motion, based on a commonly used method. We found tornadic supercells tend to move somewhat differently from the predicted motion—compared to nearby nontornadic supercells. This unusual movement often starts prior to tornadogenesis, potentially providing lead time to tornado formation. Pending further validation, development, and testing of real-time analysis tools, this storm-motion behavior could be used by operational forecasters as a factor to help determine when (or when not) to issue a tornado warning for a supercell thunderstorm, thus providing better information to the public.

KEYWORDS: Supercells; Thunderstorms; Tornadoes; Radars/Radar observations; Operational forecasting

1. Introduction

Supercell thunderstorms, characterized by a persistent rotating updraft, produce a disproportionate share of severe convective weather, including tornadoes (e.g., Moller et al. 1994). Differentiating between tornadic and nontornadic supercell environments—as well as radar signatures of these two storm classifications (Fig. 1)—remains a substantial operational forecasting and warning challenge (e.g., Markowski et al. 2011; Anderson-Frey et al. 2016; Coffer and Parker 2017; Brooks and Correia 2018; among many others). Although improvements continue to be made in understanding tornadic versus nontornadic supercell environments (e.g., Rasmussen and Blanchard 1998; Markowski et al. 2002, 2003; Thompson et al. 2003, 2012; Coffer et al. 2019), it is common for supercells to be either tornadic or nontornadic in ostensibly the same environment and/or in proximity (e.g., Fig. 1; Ziegler et al. 2001; Klees et al. 2016). Furthermore, a high percentage of supercells do not produce any tornadoes (Jones et al. 2004; Trapp et al. 2005).

Since at least the 1960s, cyclonic supercells (in the Northern Hemisphere) have been known to slow their forward movement and make a right turn early in their life cycle (e.g., right-moving supercells; Browning 1965; Browning and Foote 1976), followed occasionally by a left turn toward their demise (e.g., Fankhauser 1971), sometimes resulting in a "reverse S" storm track [Fig. 2; also see Figs. 5 and 7 in Coniglio and Parker (2020)]. Moreover, tornadoes may be more likely when supercells turn more to the right than otherwise expected and/or forecast (e.g., NOAA 2011; Coniglio and Parker 2020; Flournoy et al. 2021). Therefore, it may be possible to anticipate an increased potential for tornadogenesis when these more deviant right turns—relative to some baseline—occur with supercells. This degree of turning may yield additional information to help answer the question: "Which supercell, or supercells, in this group is more likely to become tornadic?" (as in Fig. 1).

Concordantly, supercells producing significant tornadoes (i.e., ≥F/EF2 on the Fujita/enhanced Fujita scale; Hales 1988)

Corresponding author: Matthew J. Bunkers, matthew.bunkers@noaa.gov

DOI: 10.1175/WAF-D-21-0153.1

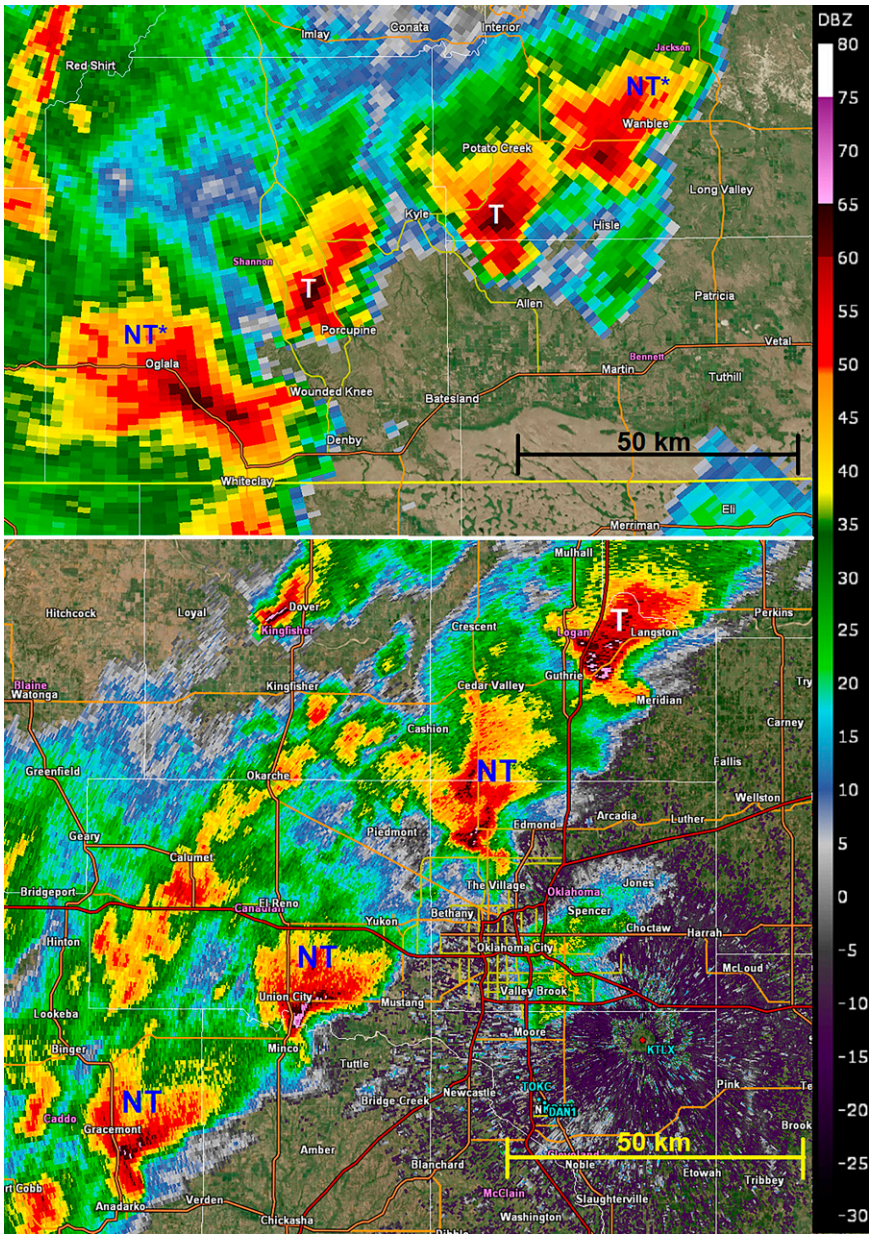

FIG. 1. (top) Rapid City, SD (KUDX), 0.5° reflectivity valid at 0027 UTC 6 Jun 1999. Only the two middle supercells were tornadic at this time, though the other two supercells produced tornadoes about 1 h prior to this time. (bottom) Twin Lakes, OK (KTLX), 0.5° reflectivity valid at 2126 UTC 10 Feb 2009. Only the far northeastern supercell was tornadic, producing five reported tornadoes between 2036 and 2237 UTC. The white "T" labels indicate tornadic supercells at this time; blue "NT" labels indicate nontornadic supercells at this time, but with an asterisk (*) if they were tornadic at some other time. The reflectivity legend (dBZ) is given at right. The background is from GR2Analyst.

tend to deviate farther away from the mean wind and perpendicular/to the right of the deep-layer shear vector than predicted by the widely used Bunkers et al. (2000) method. Two specific examples include the EF5 Joplin, Missouri, tornadic supercell on 22 May 2011 (NOAA 2011) and the F2 Superior, Nebraska, tornadic supercell on 22 June 2003 (Wakimoto et al. 2004), both of which deviated farther away from the hodograph than was forecast. In addition, Thompson et al. (2003, their Fig. 13) showed the 4–6-km storm-relative winds were stronger, on average, for significantly tornadic supercells when using the observed supercell motion versus the Bunkers et al. (2000) prediction—suggesting these supercells deviated

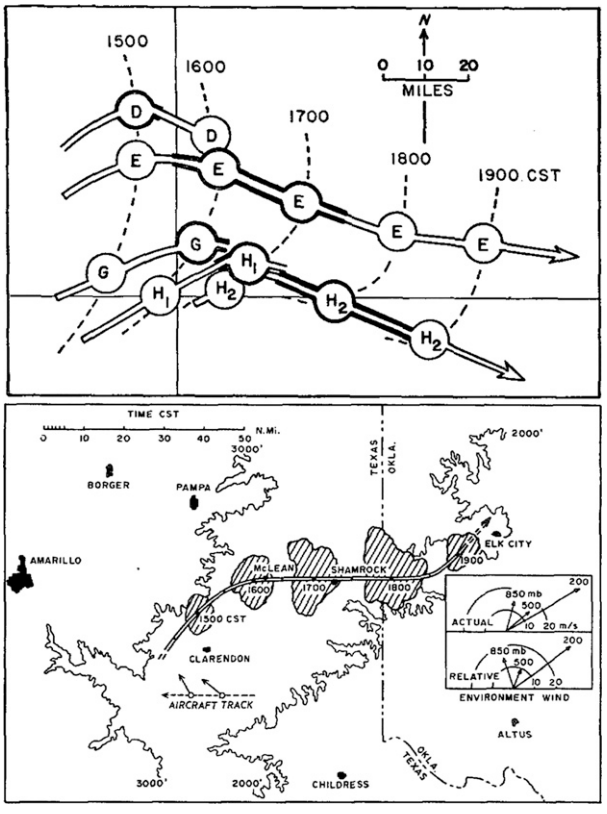

FIG. 2. (top) Schematic diagram illustrating the motion of storm cells on 26 May 1963 near Norman, OK (from Browning 1965; published 1965 by the American Meteorological Society). (bottom) Radar echo trajectory on 1 Jun 1965 over the TX Panhandle and western OK (from Fankhauser 1971).

farther off the hodograph than predicted. Using observed soundings from the Verification of the Origins of Rotation in Tornadoes Experiment 2 (VORTEX2) field project, Parker (2014, his Fig. 12) found tornadic supercells tended to deviate more strongly to the right of the hodograph than did nontornadic supercells, and a follow-up study by Coniglio and Parker (2020) made this occurrence even more apparent. Bunkers (2018) noted significantly tornadic supercells were biased 1.2 m s^{-1} slower and farther right of the hodograph than predicted by the Bunkers et al. (2000) method; this deviant motion was even more pronounced for hodographs with strong clockwise curvature and large storm-relative helicity (SRH). Finally, Flournoy et al. (2021) found that cyclonic supercells exhibiting a rightward motion, but to the left of the right-moving prediction by Bunkers et al. (2000), are less likely to be tornadic than those turning more to the right of this predicted motion.

In this exploratory study, supercells deviating off the hodograph (to the right of the shear vector) more than forecast by the Bunkers et al. (2000) method hypothetically indicate a greater tornadic potential [by enhancing the SRH and low- to midlevel storm-relative winds (e.g., Brooks et al. 1994; Coniglio and Parker 2020; Peters et al. 2020)]. Although recent studies made this connection between rightward deviant motion and increased tornadic potential over a supercell's lifetime (Bunkers 2018; Coniglio and Parker 2020; Flournoy et al. 2021), this has not been assessed with radar data on a scan-by-scan basis during various stages of tornadic and nontornadic supercells. Therefore, the objective of this study is to evaluate the radar-observed motion of supercells throughout portions of their lifetimes, and then compare that motion to the hodograph-based predicted motion from commonly used hourly operational model analyses in order to ascertain if tornadic and nontornadic supercells display notable, consistent differences. The storm-motion deviation orthogonal to the shear vector is addressed specifically. This is based on the work of Weisman and Klemp (1986, and their prior studies) showing that supercell motion is toward the right, or left, of the hodograph (0–6 km in their examples), driven largely by rotation on the flank of the storm (also see Markowski and Richardson 2010, 233–242). This type of study comparing the shear-orthogonal observed motion of supercells to the predicted motion on a scan-to-scan basis has not been undertaken for a relatively large sample of supercells, and has potential to be operationally valuable *if* the results support the above hypothesis over a diverse dataset covering multiple geographic regions. The path to operations (in terms of relevant and timely displays) would require extensive development efforts, but that is beyond the scope of this research.

2. Data and methods

The goal is to examine the motion of tornadic and nontornadic supercells that were proximate in space and time. Specifically, we desired to study the observed and predicted motion of the pretornadic through early tornadic phases of supercells, and then compare these results to those from nearby nontornadic supercells during the same hour.

a. Case selection

Initially, tornadic and nontornadic supercell cases (defined consistent with Thompson et al. 2003) were obtained from Van Den Broeke (2020), which includes 32 pretornadic and 31 nontornadic supercells during 2012–17. These cases were screened in the present study for concurrent tornadic and nontornadic supercells in the same hour (the distance criterion is discussed in section 2d), and thus not all of his cases were used. Some modifications also were made to the analysis start times based on the initial tornado report for a given supercell (see Table A1 in the appendix), which are not given by Van Den Broeke (2020). Tornado ratings and start times were determined from the National Centers for Environmental Information (NCEI) database (https://www.ncdc.noaa.gov/stormevents/), and these ratings and tornado times also were visually examined with the Storm Prediction Center (SPC) Severe Weather Browser (https://www.spc.noaa.gov/climo/online/sp3/plot.php). For 30 of the 32 pretornadic cases, there were concurrent and nearby nontornadic supercells, allowing for direct comparison of the rightward deviation between the two types of supercells for a given hour (Table A1; the KTLX case from 19 May 2013 allowed for 2 h of comparison, yielding

31 total). However, for the nontornadic cases, only three cases were obtained that had concurrent and nearby tornadic supercells in the same hour, yielding 34 (31 + 3) different hours of comparison. This was used as a proof-of-concept dataset before further data gathering was considered (Fig. 3, light green circles).

After initial testing determined this research has merit, 57 additional supercell cases from 2017 to 2020 were gathered that consist of spatiotemporally proximal tornadic and nontornadic supercell pairs and within 100 km of the closest radar (see Table A2 in the appendix). These cases were obtained by examining archived radar data on days when at least one tornado was reported. If the reported tornado was clearly produced by a supercell, and if at least one nontornadic supercell was present within a similar spatial and temporal domain (approximately less than 10 000 km^2 and storm lifetimes overlapping one another, respectively), these storms were included in a group of proximity supercells. Preference was given to the tornadic supercell with the highest initial EF-scale rating (if multiple tornadic supercells existed) when comparing to the nontornadic supercell.

Finally, 80 other supercell pairs within 200 km of the closest radar were gathered based on their significance, our awareness of them, and/or their documentation in the literature (bottom of Table A2). All of the additional 137 cases (57 + 80; Fig. 3, magenta circles) from Table A2 were combined with the 34 proof-of-concept cases (Table A1) to examine the hypothesis of this study (171 cases total). Also, unlike studies that use dual-polarization radar data and require base scans to be ≤1 km above radar level (e.g., from Table A1), supercells > 100 km from the radar were allowed for the last 80 cases in Table A2 because the methods used in the present study are relatively insensitive to a storm's distance from the radar.

b. Radar data and processing

Level II radar data were obtained from the Amazon web Services (AWS) archive (https://s3.amazonaws.com/noaa-nexrad-level2/index.html) for all cases (Tables A1 and A2) and initially screened using GR2Analyst Version 2 (http://www.grlevelx.com/gr2analyst_2/). The cases include supercells only, and generally not supercells embedded in clusters or lines because of the difficulty in deriving reliable observed storm motions with the automated storm-tracking algorithm (discussed in section 2c). However, 28 of the 171 cases (16.4%) do include supercells in clusters; clustered supercells are connected to other storms by the 40-dBZ echo for >50% of the analysis hour (for either the tornadic or nontornadic supercell, or both). Tornadoes from quasi-linear convective systems (QLCSs) were not included because supercell motion does not apply to this convective mode (unless clearly identifiable supercells with deep, persistent mesocyclones are embedded within the line).

Only the lowest scan base reflectivity (typically 0.5°) was used to track the storms. The benefit of this method is it allows for the use of supplemental adaptive intra-volume low-level scans (SAILS; Chrisman 2011) and the multiple elevation scan option for SAILS (MESO-SAILS; Chrisman 2014). SAILS was deployed in spring 2014, and MESO-SAILS was deployed in spring 2016 (J. Boettcher 2021, personal communication). These extra low-level scans can, at times, more than double the available storm-tracking information. In contrast, the WSR-88D storm-tracking algorithm (Johnson et al. 1998) uses volumetric data to create three-dimensional storm representations. Using only the lowest scan can be a problem when tracking storms close to the radar because the strongest reflectivity may be above this level. In these cases, the default reflectivity thresholds (discussed in section 2c) were reduced to ensure consistent tracking of a given storm. Prior to running the tracking algorithm, data for a given radar were interpolated to a 0.5-km grid and smoothed using a Gaussian filter with a standard deviation of 1.5 km. The Python ARM Radar Toolkit (Py-ART; Helmus and Collis 2016) was used to read the level II data and interpolate them to the grid.

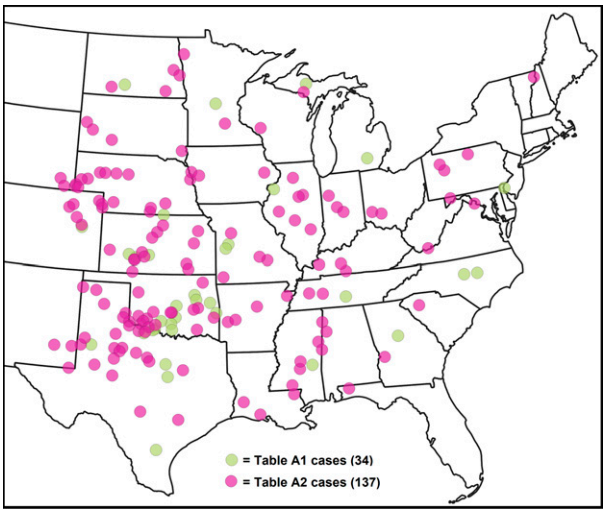

FIG. 3. Locations of the model soundings used for the concurrent tornadic and nontornadic supercell pairs for the proof-of-concept dataset (light green circles, Table A1) and larger dataset (magenta circles, Table A2).

c. Storm-tracking algorithm and storm-motion calculation

Observed motions for each supercell were calculated by using a modified version of the storm-tracking algorithm included with the differential reflectivity (Z_{DR}) arc detection algorithm presented by Wilson and Van Den Broeke (2021). This algorithm works best on isolated supercells and, on occasion, can work with supercells in clusters because it uses two reflectivity thresholds (instead of just one). It was used because of ease of application, its use of SAILS and MESO-SAILS, and also because it can be adjusted in each case, if needed, to produce accurate and consistent supercell motions required for evaluation in this exploratory study. Operational implementation of the results of this study would require a more advanced and fully automated algorithm.

This tracking algorithm first identifies storms by splitting a 45-dBZ reflectivity contour (per Wilson and Van Den Broeke 2021) into polygons and saving all polygons with an area of $\geq$10 km^2 as storm objects (Fig. 4). To account for possible embedded supercells within larger areas of convection, storm objects with areas $>$ 300 km^2 are broken into smaller storm objects by drawing a second, higher 50-dBZ[1] reflectivity contour within the large storm object and replacing the initial, large storm object with any new storm objects from this polygon (Fig. 4a, storms 1 and 2). To track storm objects from scan to scan, new storm objects are assigned a storm identification number (ID), and objects on a new scan are given the ID of the closest object within 10 km from the previous radar scan. If no object from the previous scan is located within 10 km, the storm is given a new, unique ID. To improve the tracking algorithm used by Wilson and Van Den Broeke (2021), in cases where two new storm objects are given the same ID from a previous scan, the one closest to the projected storm position from the previous scan retains that ID and the other one is given a new ID (Fig. 4b; as in Johnson et al. 1998).

The default reflectivity thresholds used to identify the storm objects (45 and 50 dBZ), the area threshold above which large storms are broken up (300 km^2), and the maximum distance new storm objects can be located from the position of a storm object at the previous scan time to be linked to (10 km) are all customizable. Such modifications, especially for reflectivity, had to be made somewhat often for supercells that were relatively weak, small, and/or close to the radar (i.e., reflectivity thresholds were lowered), as well as for stronger supercells and supercells in clusters (i.e., reflectivity thresholds typically were raised). The algorithm was not tested on small tornadic midlatitude (e.g., Davies 1990) or tropical-cyclone supercells (Edwards et al. 2012). Details on these adjustments are given in section 3a and Tables A1 and A2. Reflectivity values $<$ 20 dBZ were not used in the tracking.

For each scan, storm motion was computed for all storms that had been tracked for at least 1200 s (20 min). This time was chosen as a trade-off between too short of a period that can result in highly variable scan-to-scan storm motions and too long of a period such that changes in storm motion were overly smoothed; the goal was to represent actual short-term changes in storm motion as accurately as possible. Flournoy et al. (2021) used the past 20–25 min of instantaneous storm motion to compute the average storm motion. As a test using a longer time period, we performed a second analysis using 1800 s (30 min) as the time interval used to compute storm motion; this is discussed in the results section. Using the shorter period potentially is beneficial when supercells develop rapidly and may quickly become tornadic.

[1] The WSR-88D algorithm uses seven reflectivity thresholds of 30, 35, 40, 45, 50, 55, and 60 dBZ (Johnson et al. 1998). Moreover, the 30-dBZ threshold is applied to the minimum area of 10 km^2 for the WSR-88D (versus the default of 45 dBZ herein being applied to the same area).

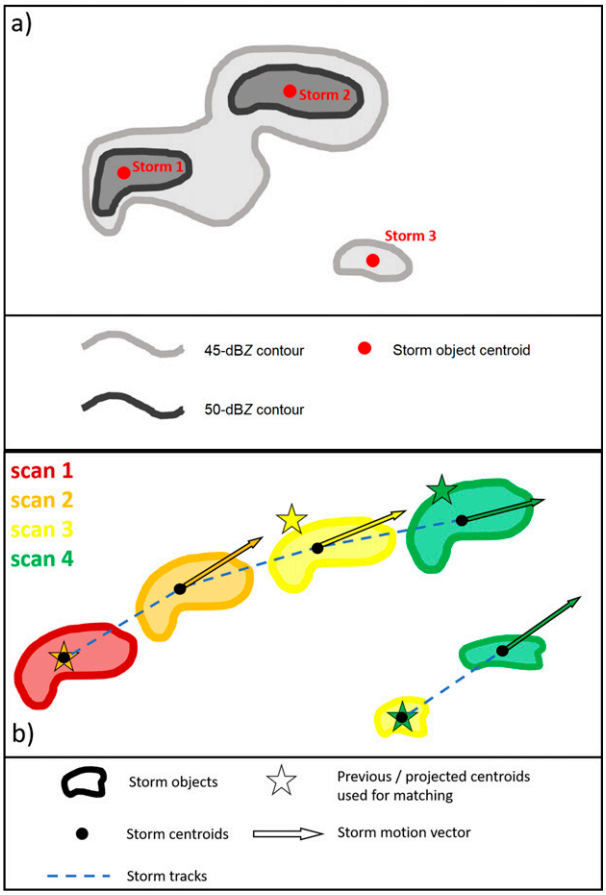

FIG. 4. Schematic illustration of the storm-tracking algorithm used in this study. (a) Reflectivity contours are broken into individual storm objects (see text for description). (b) The tracking of two idealized storms over four radar scans. The storm objects, previous/projected storm centroids used for tracking, and storm-motion vectors are colored by the radar scan they represent.

Observed storm motion was calculated each volume scan by fitting a least squares linear regression line to the storm centroid positions (for 20- or 30-min periods) and giving each point equal weight (as in Johnson et al. 1998). Once storm motions were calculated, they were used to estimate the future position of the storm (Fig. 4b). This helped keep storm IDs consistent from scan to scan. Storm tracking started 30 min before the top of the hour that contained the tornado report in order to obtain a consistent motion for the analysis, which was for the subsequent hour and 20 min (e.g., a radar analysis started at 2130 UTC for an analysis period of 2200–2320 UTC).

The sensitivity of the tracking algorithm was assessed by manually tracking a randomly selected subset of 10 supercells. The automated and manual tracking are fairly similar, with the mean difference of 0.67 m s^{-1} and the 75th percentile difference remaining below 1 m s^{-1}. The largest differences occur with storms that undergo a merger, which also can result in varying manual analyses. No bias is present in the

results between the automated and manual tracking for this small subset.

d. RUC/RAP model soundings and proximity considerations

Sounding profiles from the Rapid Update Cycle (RUC; Benjamin et al. 2004) or the Rapid Refresh (RAP; Benjamin et al. 2016) operational models were obtained for this analysis; the RAP replaced the operational RUC in May 2012. So-called proximity soundings (Parker 2014; Wade et al. 2018) were determined by selecting a point in the storm inflow region 40–80 km away from the storm as suggested by Potvin et al. (2010). These soundings were constructed from the postprocessed 25-hPa vertical levels at the model grid point closest to the desired location. For the most part, profiles were obtained at 60 km from the edge of a storm's reflectivity gradient, but this was adjusted slightly closer or farther away to avoid influence from other storms that may have been in the area (observed via GR2Analyst) in order to sample a non-contaminated near-storm environment; the model profiles also were examined to remove those potentially contaminated by model-based storms (e.g., looking for saturated or moist-adiabatic layers). Soundings were obtained for the start of the analysis hour and were considered valid for the radar data from −30 min to 1 h 20 min from that time (i.e., only one forecast supercell motion was used for each case); this permitted the algorithm to be run continuously for nearly a 2-h period. All soundings were visually examined and required to have (i) positive CAPE using the lowest 300-hPa most-unstable parcel and (ii) a wind profile representative of the storm inflow (as opposed to shallow postfrontal or outflow environments).

Concurrent tornadic and nontornadic supercells needed to have 20–60 min of their life cycle occur within the same hour in order to be considered, consistent with the shortest storm-motion calculation duration. Ideally, both supercells' lifetimes overlapped the entire hour. Next, the supercells were required to be <120 km apart at the time of the inflow sounding, which allowed for the sounding to be within 60–80 km of each supercell, consistent with Potvin et al. (2010). Although considerable mesoscale variability can exist over this distance (and time, noted in the prior paragraph), deep-layer bulk shear and the mean wind are relatively consistent over these scales compared to other variables such as SRH (Markowski et al. 1998; Coniglio and Parker 2020, their Fig. 4). Moreover, supercell motion can be relatively steady across larger time and space domains than those used herein (e.g., Klimowski and Bunkers 2002, their Fig. 3)—especially from a perspective moving with the storm. If the results of this exploratory study eventually get implemented operationally, inclusion of gridded model output (e.g., possibly with hourly to subhourly supercell-motion predictions available every 3 km in the x and y directions) instead of a single sounding would help refine environmental input into the deltas algorithm (discussed next).

e. Definition of supercell-motion "deltas"

The unmodified Bunkers et al. (2000) algorithm was used to compute the forecast supercell motion (from the hourly RUC/RAP profiles) because of its widespread use and simplicity (Ramsay and Doswell 2005; Bunkers et al. 2014). This algorithm assumes supercell motion is the sum of (i) advection by the mean wind and (ii) propagation away from the mean wind, purely normal to the deep-layer shear vector [Fig. 5; also see Zeitler and Bunkers (2005, their Fig. 2)]. Bunkers et al. (2000) used 7.5 m s^{-1} for the propagation component (dotted green arrow in Fig. 5) because it minimized the bulk forecast motion error, but they reported a large range of deviations from 3 to 18.5 m s^{-1}. This baseline prediction (Fig. 5) is used below (as shown in Fig. 6) to compute tornadic and nontornadic supercell storm-motion deviations (relative to the 7.5 m s^{-1} propagation component) along the shear-orthogonal direction (dotted green arrow in Fig. 5).

The radar-observed supercell motion, as well as the hourly RUC/RAP forecast supercell motion derived from model-analysis soundings, were compared on a scan-by-scan basis by computing both (i) the mean absolute error (MAE) between the two supercell-motion vectors (radar-observed versus forecast RUC/RAP) and (ii) a shear-relative deviation perpendicular to the deep-layer shear vector (hereinafter referred to as "deltas"). The first metric (MAE) is determined by taking the difference between the predicted "Right Mover" (square) and "Observed" (X) markers in Fig. 6 (dashed gray vectors), whereas the storm-motion deltas are represented by the blue and red vectors in Fig. 6. These deltas are calculated as the *shear-orthogonal distance* between the observed and Bunkers et al. (2000) forecast supercell motions (negative toward the left of the Bunkers et al. prediction), where the shear vector is defined over the 0–0.5- to 5.5–6-km layer.[2] MAEs are always greater than or equal to the deltas (Fig. 6). Based on this definition, the deltas are hypothesized to be the more critical parameter based on supercell dynamics (e.g., Weisman and Klemp 1986; Markowski and Richardson 2010, 233–242)—versus the MAEs—with tornadic supercells deviating more strongly to the right of the shear vector (consistent with the red arrows) versus less deviation for the nontornadic supercells (consistent with the blue arrows). Moreover, the results below show the most important metric for a given supercell environment is the relative difference between the deltas (e.g., a tornadic supercell having larger deltas than a nearby nontornadic supercell).

Finally, sensitivity tests were performed by evaluating shallower shear layers (0–3 and 0–1 km) for computing the deltas, and comparing the results to those from the default

[2] The 0–0.5- to 5.5–6-km shear vector was chosen because it was used in Bunkers et al. (2000). The choice was made therein to average the head and tail of the shear vector to account for noise/variability (i.e., a 500-m layer average in this case). Rasmussen and Blanchard (1998) similarly defined their deep-layer shear vector by using a 0–0.5-km average for the head. Hereafter, this layer is simply referred to as the 0–6-km shear layer. Nevertheless, operational implementation of the deltas technique using the simple 0–6-km shear layer would be an adequate proxy.

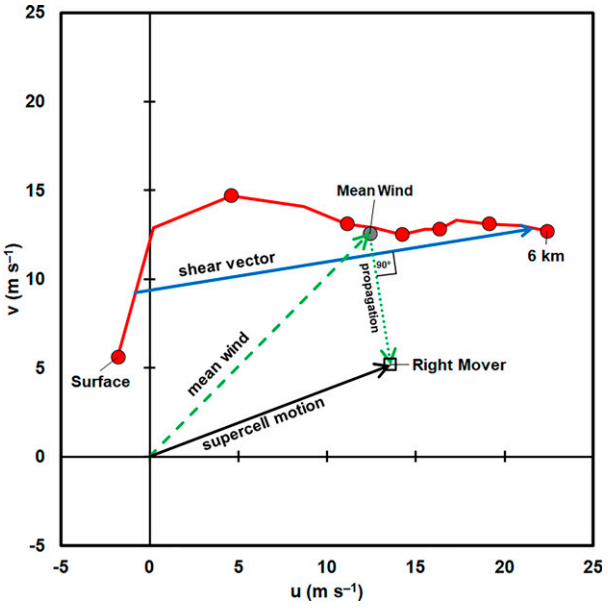

FIG. 5. Surface–6-km hodograph (red, circles every 1 km) depicting the calculation of the right-moving supercell motion from Bunkers et al. (2000). The propagation vector (dotted green arrow) is 7.5 m s^{-1}.

0–6-km layer.[3] The baseline Bunkers et al. (2000) supercell-motion prediction algorithm (using the 0–6-km layer) still was used for all storm-motion calculations; the shear layer was changed only for computing the deltas after the supercell-motion prediction was calculated. These shallower shear layers may be relevant to the deltas when considering (i) the importance of low-level shear/SRH to mesocyclone strength and tornadogenesis (e.g., Markowski et al. 2003; Coffer and Parker 2017; Coffer et al. 2019; Peters et al. 2020) and (ii) very shallow supercells.

f. Analysis of supercell-motion deltas and MAEs

Four specific comparisons of the storm-motion deltas and MAEs for the tornadic and nontornadic supercells were assessed. Statistical significance for the differences in means or medians were calculated, where appropriate, using the Wilcoxon–Mann–Whitney (WMW) rank-sum and Wilcoxon (W) signed-rank tests (Wilks 1995), the two-sample Kolmogorov–Smirnov (KS) test (Wilks 1995), and a *t* test for the distribution of differences between tornadic and nontornadic pairs (Milton and Arnold 1990; also see Bunkers et al. 2000). The first three tests are nonparametric and thus do not depend on the underlying data distribution; the first two tests also are resistant to outliers. The *t* test requires the differences to follow a Gaussian distribution. The recommended settings for the various analyses (e.g., storm-motion calculation duration, shear-layer depth for the deltas) were determined by using a combination of these statistical tests.

For the first comparison, the average, median, and maximum for each member of the supercell pair (tornadic and nontornadic) were directly compared during their overlapping time interval (up to 1 h). This was done for both the deltas and MAEs as defined in section 2e. Second, the average deltas for up to 30 min (consistent with Van Den Broeke 2020) prior to the first tornado (depending on when tornadogenesis occurred in the radar analysis period) were compared to the average deltas for the same period following the first tornado start time; this also was repeated for the MAEs. Third, the average delta *trend* for up to 30 min prior to tornado formation was compared to the average delta trend during the same period following the first tornado start time. Finally, the linear correlation coefficient was calculated between the median delta and the maximum EF-scale rating for a given tornadic supercell. We did not examine each 1-min tornado-rating segment because of the lack of damage indicators of sufficient density and strength, as well as the subjectivity of the rating process (e.g., Doswell and Burgess 1988; Edwards et al. 2013; Wurman et al. 2021). Using the maximum EF-scale rating alleviates some, but not all, of these concerns. EF-unknown (EFU) ratings were not used for this specific analysis; furthermore, a 2-min window was used to match a radar scan to a tornado report. These analyses helped determine whether (i) tornadic supercells tend to deviate more to the right of the hodograph while they are producing tornadoes compared to nearby nontornadic supercells, (ii) tornadic supercells trend toward larger deviation to the right of the hodograph during the period up to 30 min prior to producing a tornado versus following tornadogenesis, and (iii) the magnitude of rightward deviation of tornadic supercells is related to tornado damage rating.

3. Results

The first case in Table A1 is used here to illustrate the process of calculating the various statistics for the supercell-motion deltas and MAEs. First, the radar data were processed with the storm-tracking algorithm, producing radar-like object displays of the 40-dB*Z* storm outlines and associated storm IDs for each 0.5° scan (e.g., Fig. 7a, near the time of tornadogenesis; #16 was tornadic and #17 was nontornadic). Storm IDs were color coded and scaled by the delta magnitude for ease of interpretation. Large red IDs portray large deltas whereas smaller and/or green IDs portray smaller deltas; very small green IDs often were associated with left-moving supercells. Next, common periods of analysis were determined for the tornadic (Fig. 7b) and nontornadic supercells (Fig. 7c). In this case, both storms (#16 and #17) have data for the entire 1-h period starting at the top of the analysis hour (2300–0000 UTC). The deltas and MAEs during this common period were used to compute averages, medians, and maximums for each pair, and this was done for each case in Tables A1 and A2, which then were used for validation in

[3] We also tested the effective bulk wind difference (EBWD; Thompson et al. 2007) layer based on a comment from an internal reviewer, which also was suggested by one of the peer reviewers. The results for the EBWD layer were nearly identical to those for the 0–6-km layer (i.e., differences mostly <0.1 m s^{-1}), and only 2%–4% better discrimination using the 0–6-km layer). Therefore, no further discussion of the EBWD layer is presented.

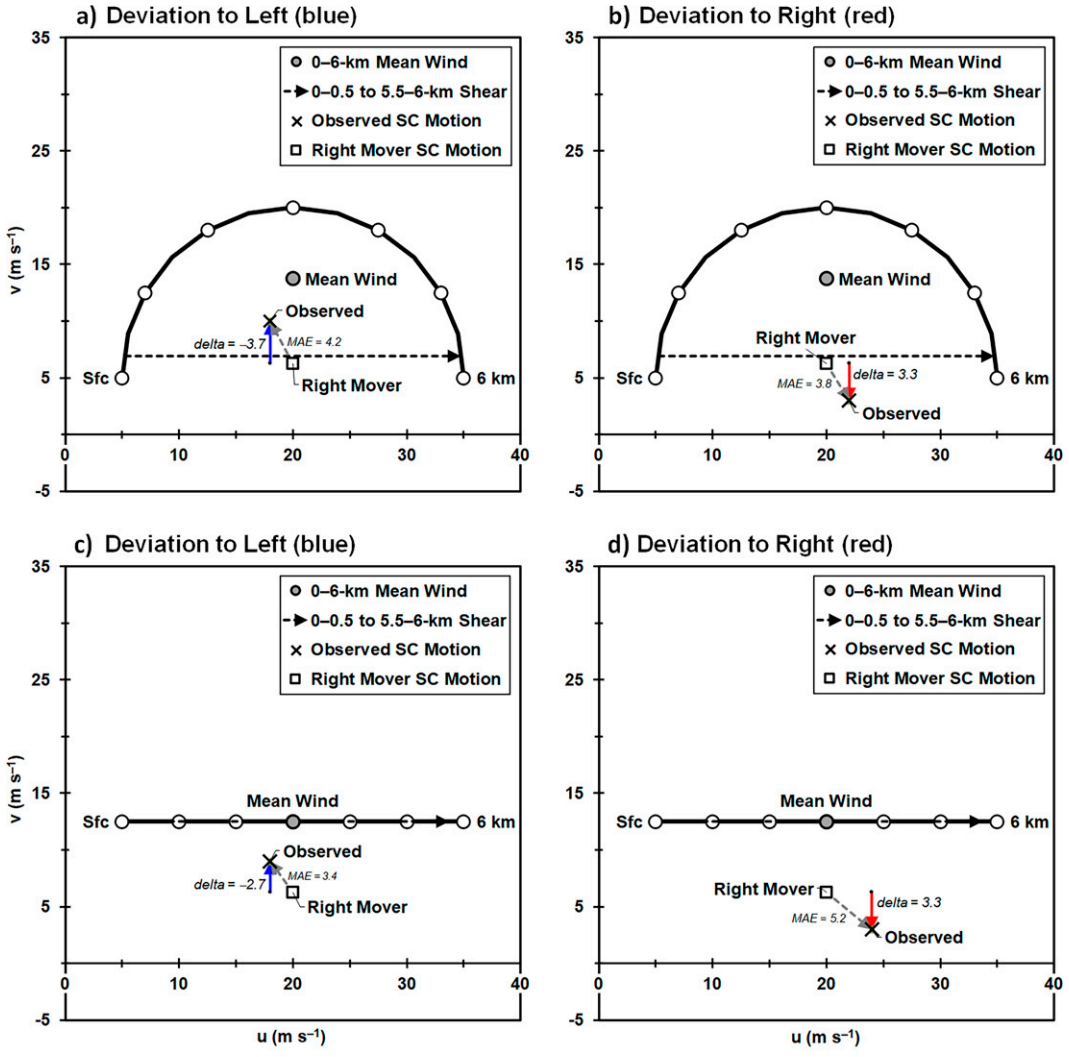

FIG. 6. Idealized hodographs depicting shear-orthogonal supercell (SC) motion deviation (i.e., "deltas") toward the left or right of the Bunkers et al. (2000) "Right Mover" prediction (square) for a (a) curved hodograph with storm-motion deviation toward the left of the square, (b) curved hodograph with storm-motion deviation toward the right of the square, (c) straight hodograph with storm-motion deviation toward the left of the square, and (d) straight hodograph with storm-motion deviation toward the right of the square. The supercell-motion "deltas" (red and blue vectors) and MAEs (dashed gray vectors) are labeled per the discussion in section 2e. The hodographs and shear vectors overlap in (c) and (d).

the following sections. In addition, supercell-motion deltas and MAEs were averaged for equal periods (up to 30 min) depending on the time with overlapping data before and after the start of the first tornado; this was 18 min in this case (2342–2400 UTC versus 0000–0018 UTC). As mentioned previously, the averaging period for some cases was constrained by the existence of other supercells and available radar data, with the minimum period of about 15 min. At least 95% of the 171 cases had ≥18 min of overlap, 75% had ≥27 min of overlap, and 50% had ≥30 min of overlap. Trends in the deltas also were computed for the same "before and after" periods. Finally, median deltas were matched to the maximum EF-scale for tornadoes occurring in the same 1-h period as above; thus, for Fig. 7b the median delta of 0.128 m s^{-1} was matched to the EF0 tornado report. Sections 3a–3i below discuss the results from the combined cases in Tables A1 and A2.

a. *Tracking algorithm*

The default reflectivity thresholds for the tracking algorithm (45 and 50 dB*Z*) were appropriate for 44.1% and 53.3% of the cases in Tables A1 and A2, respectively. These thresholds were adjusted incrementally either upward or downward 1–2 dB*Z* when the defaults did not result in consistent storm IDs during the tracking period (i.e., changing of storm IDs for the same storm). Regarding the cases in

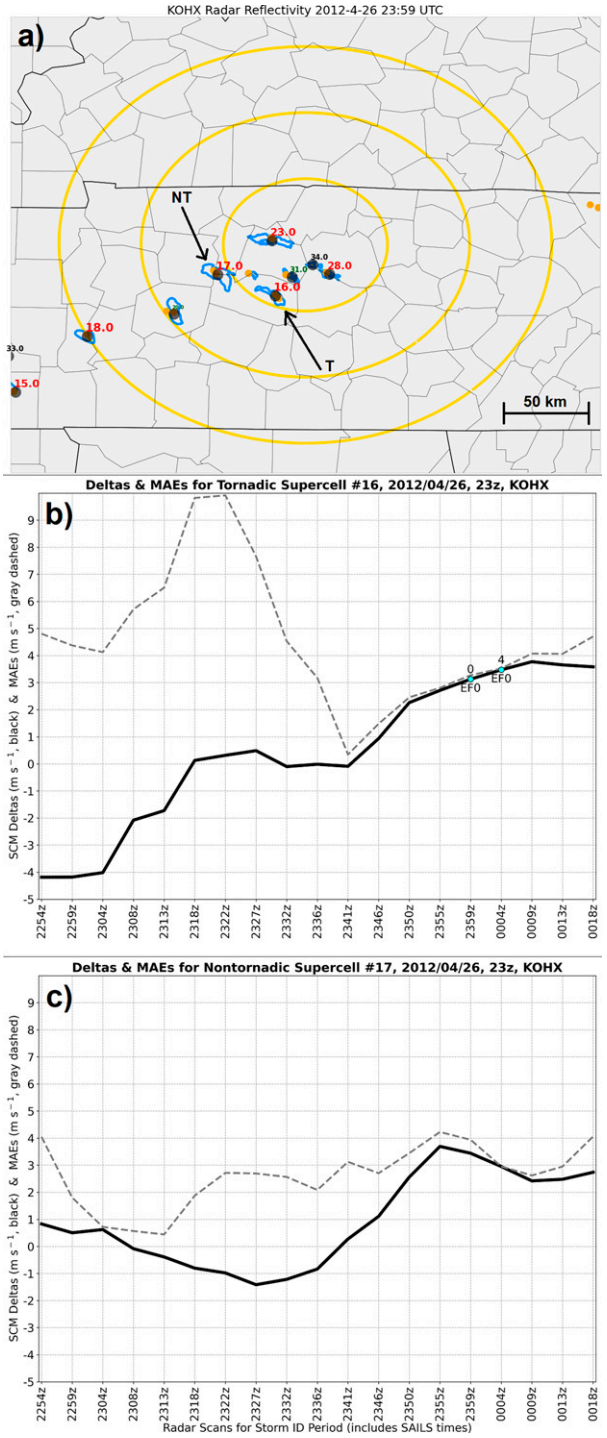

FIG. 7. Example using the first case in Table A1 (KOHX, 26 Apr 2012) to illustrate the process of calculating the various statistics for the supercell-motion deltas and MAEs (using a 20-min storm-motion duration and the 0–6-km shear layer for the deltas). (a) The 40-dB*Z* reflectivity outlines in cyan, black storm IDs are for newer storms with insufficient data to calculate a storm motion, red storm IDs are for storms with positive deltas, green storm IDs are for storms with negative deltas, and yellow range rings are at 50, 100, and 150 km. The red and green storm IDs are scaled by the magnitude of the deltas. Black arrows point toward tornadic (T) and nontornadic (NT) supercells. (b) A time series of the deltas (black line) and MAEs (dashed gray line) for tornadic storm #16 in (a); and (c) as in (b), but for nontornadic storm #17. Tornado EF-scale ratings and times (nearest minute) are plotted for the 0.5° scans in (b). No smoothing has been applied to either of the time series; they are based on the storm motion calculated at each volume scan.

Table A2, 35%–40% of the initial candidate pairs of tornadic and nontornadic supercells were discarded (and not included in Table A2) because the tracking algorithm could not track the individual storms for a sufficient time (i.e., ≥20 min during the primary analysis hour). Operational implementation of the delta algorithm would require more advanced routines to automatically track three-dimensional cells (e.g., Johnson et al. 1998; Cintineo et al. 2020), and possibly a filter for supercell/mesocyclone identification (e.g., Stumpf et al. 1998).

b. *Storm-motion calculation duration*

The storm-motion calculation duration results do not favor either of the 20- or 30-min settings in distinguishing between tornadic and nontornadic supercells (Table 1, right two columns). For example, the average deltas (each averaged over the 171 cases) for the tornadic cases were slightly larger for the 20- versus 30-min values (0.541 versus 0.472 m s^{-1} in Table 1), yet the tornadic minus nontornadic average deltas only slightly favored the 30-min duration (1.902 versus 1.926 m s^{-1} in Table 1). These small differences between the 20- and 30-min storm-duration results hold as well for the other two shear layers that were tested (Fig. 8). These small differences between the 20- and 30-min results are not statistically significant. Given these small differences, and considering a shorter averaging time is better for gaining lead time on newly and/or quickly developing storms (as in Flournoy et al. 2021)—as well as on existing quasi-steady storms that suddenly intensify—it makes sense to use the 20-min averaging period for the storm-motion calculation. The main advantage of using the 30-min averaging period is that the deltas (and MAEs) do not show as much scan-to-scan variability when compared to the 20-min period (e.g., compare the maximum average deltas between the 20- and 30-min data in Table 1). However, this variability is not as important compared to lead time for potential real-world warning decision-making applications.

c. *Supercell-motion deltas versus MAEs*

When evaluating the efficacy of the deltas and the MAEs (for 20- and 30-min storm-motion calculations), delta magnitudes for average, median, and maximum are larger for the tornadic versus nontornadic supercells (ranging from 1.902 to 2.052 m s^{-1} larger; third column and top half of Table 1), whereas the MAEs are negative (and smaller absolute magnitude) for the tornadic versus nontornadic supercell comparisons (ranging from −0.364 to −0.728 m s^{-1}; third column and bottom half of Table 1). The deltas are larger for the tornadic versus nontornadic supercells 77.8%–81.3% of the time for the average, median, and maximum deltas (Table 1, right

TABLE 1. Averages for supercell-motion (SCM) deltas (top half of table) and mean absolute errors (MAEs; bottom half of table) for the 171 cases in Tables A1 and A2. Averages (top number in each group), medians (middle number in each group), and maximums (bottom number in each group) were computed for overlapping periods of the tornadic and nontornadic supercell pairs. The deltas are based on the 0–6-km shear layer (shear6) using 20- and 30-min durations for the storm-motion calculations. Superscripts denote p values that are <1% for the 1) WMW, 2) W, 3) KS, and 4) t tests for the differences.

	Tornadic averages (m s^{-1})	Nontornadic averages (m s^{-1})	Tornadic minus nontornadic (m s^{-1})	Percent tornadic > nontornadic
		SCM delta averages		
shear6, 20 min				
Average	0.541	−1.361	1.902[1,2,3,4]	81.3%
Median	0.562	−1.383	1.945[1,2,3,4]	77.8%
Max	3.236	1.240	1.995[1,2,3,4]	76.0%
shear6, 30 min				
Average	0.472	−1.455	1.926[1,2,3,4]	80.1%
Median	0.528	−1.400	1.928[1,2,3,4]	79.5%
Max	2.492	0.440	2.052[1,2,3,4]	78.9%
		SCM MAE averages		
shear6, 20 min				
Average	4.865	5.296	−0.431	45.0%
Median	4.786	5.150	−0.364	43.9%
Max	8.091	8.706	−0.615	40.9%
shear6, 30 min				
Average	4.623	5.136	−0.514[2,4]	43.9%
Median	4.548	5.005	−0.457	40.9%
Max	7.100	7.829	−0.728	41.5%

column and top half), compared to only 40.9%–45.0% of the time for the MAEs (i.e., minimal discrimination skill at best). Using one-sided tests (based on the hypothesis herein), p values are <1%, indicating statistical significance, for all of the tests for the deltas (top half of Table 1), whereas p values are mostly >1% for the analogous MAE tests. This reveals skill in discriminating tornadic versus nontornadic supercells when using the delta parameter relative to the MAE.

Although both the deltas and MAEs are from 0.384 to 0.961 m s^{-1} larger after tornadogenesis compared to the same period prior to tornadogenesis (Table 2, right column), the change in MAE after tornadogenesis is related mostly to the shear-orthogonal deviation (i.e., the deltas). Moreover, the increase in the average deltas (for after versus before the first tornado) is from 0.198 to 0.469 m s^{-1} larger than for the increase in MAEs. Therefore, supercell-motion deltas are more relevant than MAEs with respect to differentiating between tornadic and nontornadic supercells, which is consistent with previous studies (e.g., Coniglio and Parker 2020, their Fig. 8). These results may be meaningful prior to the first tornado of the day when discriminating tornadic potential between adjacent supercells is especially challenging (e.g., Krocak et al. 2021).

d. Shear layer for delta calculation

Figure 8 shows that the 0–6-km shear layer is only slightly favored over the 0–3-km layer for computing the deltas. The difference in storm-motion delta magnitudes between tornadic and nontornadic supercells shows a small decrease from the 0–6- to 0–3-km layers, and a more notable decrease from 0–3 to 0–1 km. For example, the average tornadic delta differences decrease from 1.902 to 1.751 to 0.954 m s^{-1} (for these three shear layers using the 20-min storm-motion calculation). Using the 0–1-km shear layer to compute the deltas results in some discriminatory ability (60%–65%) between tornadic and nontornadic supercells (green violin plots in Fig. 8; highest p value of all four tests = 0.98%), whereas the 0–6-km shear layer yields ≥80% of the cases with larger average deltas for the tornadic supercells (magenta and red violin plots; highest p value of all four tests = 0.001%). Although the shallowest shear layer (≤0–1 km) has been found to be critical for tornadogenesis (refer to section 1), the overall storm-motion deviation—as related to tornadogenesis—is better represented by a deeper layer (e.g., 0–6 km). This is consistent with the importance of the midlevel mesocyclone in the supercell tornadogenesis process (e.g., Markowski and Richardson 2009), as well as the interaction of the deeper column updraft with the deeper shear layer to generate greater flanking pressure-gradient forces. This highlights the complex nature of supercell physical processes occurring through a deep layer that can impact tornadogenesis.

e. Supercell-motion delta trends before and after tornadogenesis

As noted above, supercell-motion deltas are about 1.9–2.0 m s^{-1} larger, on average, for tornadic versus nontornadic supercells (Table 1), and supercell-motion deltas are about 0.9 m s^{-1} larger, on average, after tornadogenesis versus before (Table 2). But what about the *trends* in the deltas prior to and after tornadogenesis? The hypothesis was that the trends would be more positive (i.e., increasing faster) before tornadogenesis than after, and this is somewhat apparent in the results for the 0–6- and 0–3-km shear layers (Table 3, about 57% of the time). These two shear layers perform

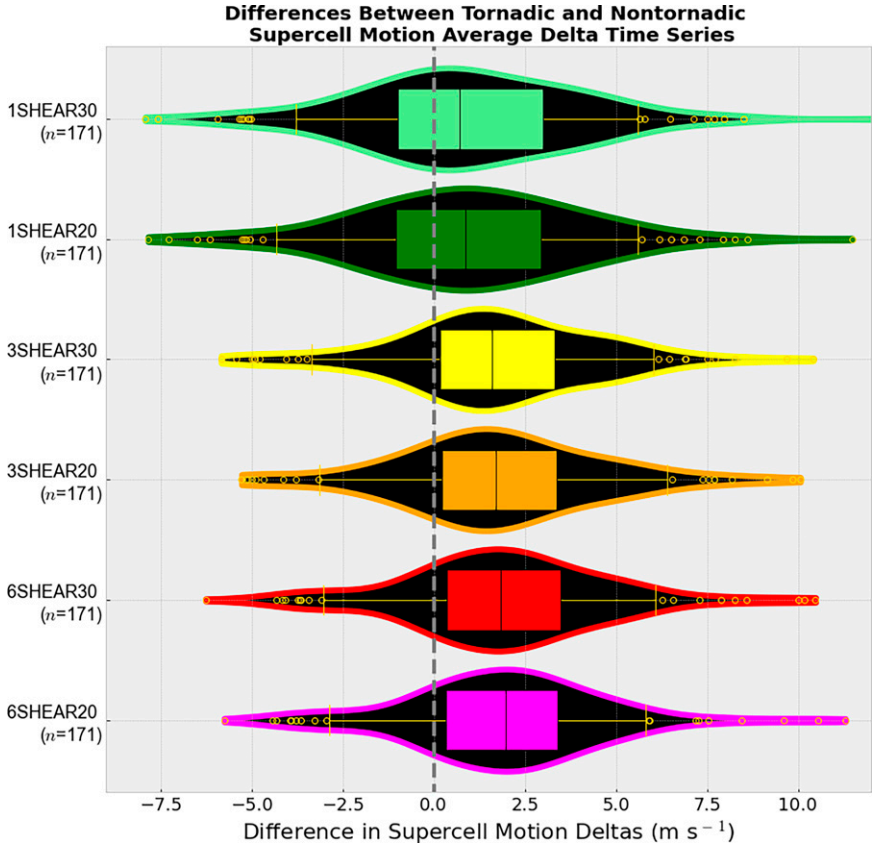

FIG. 8. Violin plots of the difference in average supercell-motion deltas between the 171 tornadic and nontornadic supercell pairs from Tables A1 and A2. For each plot, the box extends from the 25th to the 75th percentile of the data, with the median represented by the middle line. The two lines past the edges of the box extend to the 5th and 95th percentiles, and the open yellow circles mark outliers beyond that range. The 6SHEAR20 label denotes the 0–6-km shear layer for the deltas using 20 min for the storm-motion calculation; the other labels are analogous. Positive deltas represent greater average shear-orthogonal rightward deviations for the tornadic supercells.

nearly the same for the 20- and 30-min storm-motion calculations, respectively. The trend of 0.045–0.046 m s^{-1} min^{-1} equates to a 0.7–1.4 m s^{-1} average increase in shear-relative rightward deviation leading up to tornadogenesis. Even though the trends remain positive after tornadogenesis for the 30-min storm-motion calculation (at 38% of the pretornadic magnitude), they decrease to 11% of the pretornadic magnitude for the 20-min storm-motion calculation. The shorter 20-min averaging period makes the change/difference in trend magnitudes before and after tornadogenesis more apparent. The trends are positive 62%–70% of the time prior to tornadogenesis, thus indicating that increased deviation toward the right of the Bunkers et al. (2000) prediction often starts at least 15 min (near the minimum overlapping period

TABLE 2. As in Table 1, but for average deltas and MAEs before and after the first tornado in a given hour. Averages were computed for the same duration (up to 30 min) both before and after tornadogenesis for a given case. The deltas are based on the 0–6-km shear layer (shear6) using 20- and 30-min durations for the storm-motion calculations. Superscripts denote p values that are <1% for the 1) WMW, 2) W, 3) KS, and 4) t tests for the differences.

	Average before first tornado (m s^{-1})	Average after first tornado (m s^{-1})	After minus before (m s^{-1})
		SCM delta averages	
shear6, 20 min	0.221	1.074	$0.853^{1,2,4}$
shear6, 30 min	0.105	1.066	$0.961^{1,2,3,4}$
		SCM delta MAEs	
shear6, 20 min	4.438	4.822	0.384
shear6, 30 min	3.853	4.616	$0.763^{1,2,3,4}$

TABLE 3. As in Table 2, but for average delta trends (m s^{-1} min^{-1}) before and after the first tornado in a given hour. Trends were computed for the same duration both before and after tornadogenesis for a given case. The deltas are based on the 0–6- (shear6) and 0–3-km shear layers (shear3) using 20- and 30-min durations for the storm-motion calculations. Superscripts denote p values that are <1% for the 1) WMW, 2) W, 3) KS, and 4) t tests for the differences.

SCM delta averages	Average trend before first tornado	Average trend after first tornado	Trend (before minus after)	Percent cases trend before > trend after
shear6, 20 min	0.045	0.005	$0.040^{1,2,3,4}$	57.1%
shear6, 30 min	0.037	0.014	$0.023^{1,2,3}$	56.3%
shear3, 20 min	0.046	0.005	$0.041^{1,2,3,4}$	57.6%
shear3, 30 min	0.037	0.014	$0.023^{1,2,3,4}$	57.0%

for a given case prior to and after tornadogenesis) to 30 min [consistent with Van Den Broeke's (2020) pretornadic period] prior to tornadogenesis (Fig. 9).

f. *Correlation between maximum EF-scale ratings and median deltas*

The linear correlation coefficient between the maximum EF-scale rating and median supercell-motion delta for each tornadic supercell shows a modest positive relationship (r = 0.164; Fig. 10); the 1-sided p value is 0.018. There is a slight signal for stronger tornadoes (>EF1) to be associated with larger delta values, but this may partially be a result of the small sample size (Doswell 2007) at higher EF-scale ratings (only 49, or 30.1%, of the data points are >EF1). The average median delta for weak (EF0/1) tornadoes is 0.21 m s^{-1}, whereas the average median delta for the EF2–4 tornadoes is 1.01 m s^{-1}. There also is large variance in the deltas, especially at the EF0 scale, which is consistent with non-damage-producing tornadoes being logged as EF0 (Edwards et al. 2021). If the EF0 tornadoes and outlier EF5 are disregarded, the weak positive correlation increases to 0.283 (Fig. 10, dashed gray line; p = 0.003), overall supporting a positive relationship between greater shear-orthogonal rightward deviation as EF-scale rating increases.

g. *Relative differences between tornadic and nontornadic supercell-motion deltas*

There are 75 negative delta values (or 46.0%) associated with the tornadic phase of several of the supercells (Fig. 10). A closer inspection reveals that the relative difference in deltas between the tornadic and nontornadic supercells may be more meaningful to consider (Fig. 11). For example, there are 53 tornadic cases with negative average deltas (out of a total of 75) that still are larger than the associated deltas from the nearby nontornadic supercells. Indeed, only 18.7% of the 171 cases exhibited larger average deltas for the nontornadic supercell. These results are consistent with Bunkers et al. (2000), who noted wide variability in deviations from the mean wind compared to the prescribed 7.5 m s^{-1} value for supercell-motion prediction—suggesting tornadic deltas need

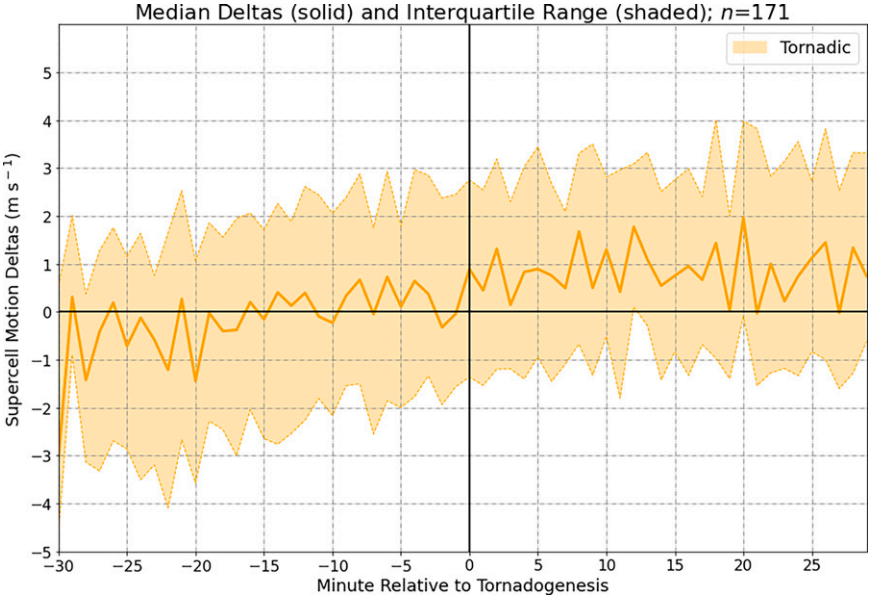

FIG. 9. Time series of the median tornadic supercell-motion deltas for all 171 cases centered on ±30 min of the first tornado (for the 0–6-km shear layer and 20-min storm-motion calculation). The interquartile range (middle 50%) is shaded.

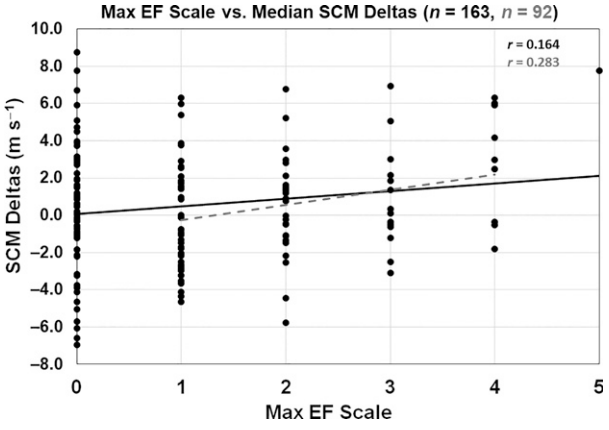

FIG. 10. Scatterplot of maximum EF-scale rating vs median supercell-motion (SCM) deltas (m s^{-1}) for the 163 cases with non-EFU ratings in Tables A1 and A2 (for the 0–6-km shear layer and 20-min storm-motion calculation). The black line is the best linear fit to the data, with a correlation coefficient (r) of 0.164; the dashed gray line is the same, but for the EF1–4 tornadoes (r = 0.283).

not always be positive. Thus, even when tornadic supercell motions were to the left of the original Bunkers et al. (2000) estimate (e.g., as in the Figs. 6a,c idealized hodographs), they still usually were to the right of nearby nontornadic supercell motions.

h. *Changes in supercell-motion deltas with time*

The relative difference in tornadic versus nontornadic deltas also was apparent in time. Specifically, the delta differences were more noticeable after the first 15 min of the analysis hour (HH:00 to HH:59, Fig. 12), at which time 24.6% of the tornadic supercell cases had produced their first tornado. There is slightly less than a one-quartile offset in the distributions after 15–20 min (Fig. 12a, gray shading) but less offset in the first 15 min (i.e., the orange and blue lines are relatively close during this time). The 95% confidence intervals around the median also overlap considerably in the first 10–15 min (Fig. 12b) but with very little overlap thereafter (per the white space between the time series).

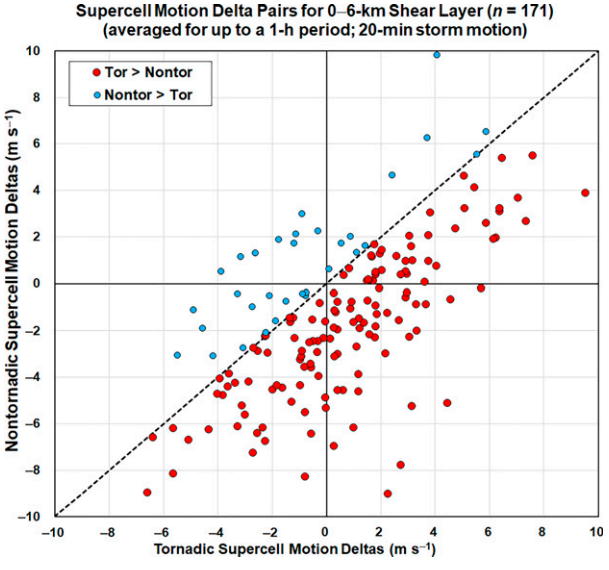

FIG. 11. Scatterplot of tornadic supercell-motion deltas vs nontornadic supercell-motion deltas (m s^{-1}) for the 171 cases in Tables A1 and A2 (for the 0–6-km shear layer and 20-min storm-motion calculation). The black dashed line is the 1-to-1 line separating the deltas for tornadic > nontornadic (red, 81.3% of the cases) and nontornadic > tornadic (cyan, 18.7% of the cases).

i. *Supercell-motion deltas versus time of day*

In addition to the above analyses, storm-motion deltas were examined by time of day for all 171 cases, because deltas were hypothesized to decrease during the early evening as the nocturnal oscillation-driven low-level jet (LLJ) typically intensifies (e.g., Shapiro et al. 2016; Parish 2017)—common across the plains and upper Mississippi Valley regions in the warm season. This occasionally can lead to supercells turning left of their usual rightward deviation after the LLJ increases (e.g., Bluestein et al. 2019, their Fig. 8). The onset of the nocturnal inversion also may affect the rightward deviation of

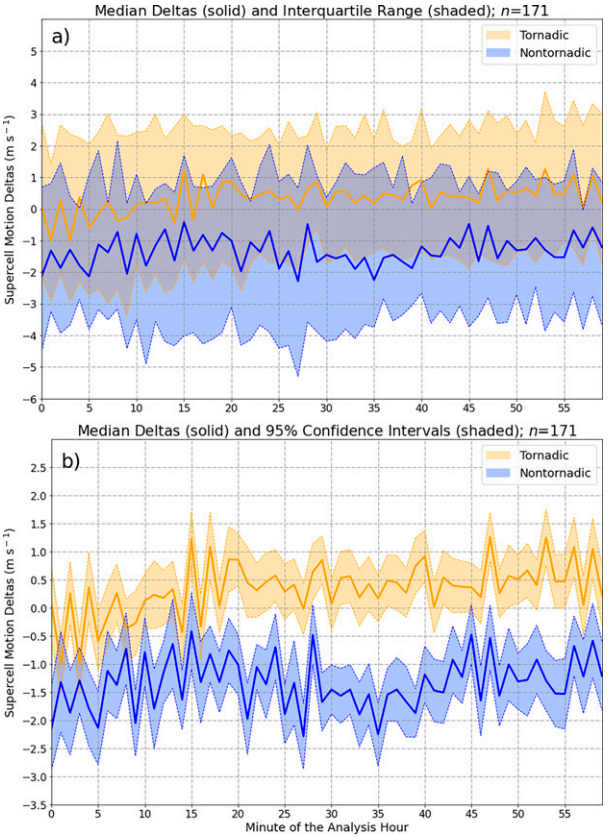

FIG. 12. Time series of the median supercell-motion deltas for all 171 cases for the tornadic (orange) and nontornadic (blue) supercells (for the 0–6-km shear layer and 20-min storm-motion calculation). (a) The interquartile range (middle 50%) is shaded and (b) the 95% confidence interval about the median is shaded.

supercells, especially as they possibly become elevated (e.g., Nowotarski et al. 2011; Bunkers et al. 2014). Accordingly, the average deltas from 1900 to 2300 UTC were 0.82 m s^{-1}, but from 0000 to 0400 UTC they were 0.22 m s^{-1} (Fig. 13)—a decrease of −0.60 m s^{-1} from the previous period. The difference in means, however, is not statistically significant. Conversely, the nontornadic deltas increased slightly (0.14 m s^{-1}) during this same time (possibly because these storms were more elevated), from −1.35 to −1.21 m s^{-1}. The average delta differences between tornadic and nontornadic supercells were greatest during the afternoon (2.17 m s^{-1})—relative to the evening (1.43 m s^{-1})—consistent with boundary layer decoupling, an increasing low-level jet, and greater LCL–LFC separation during the evening.

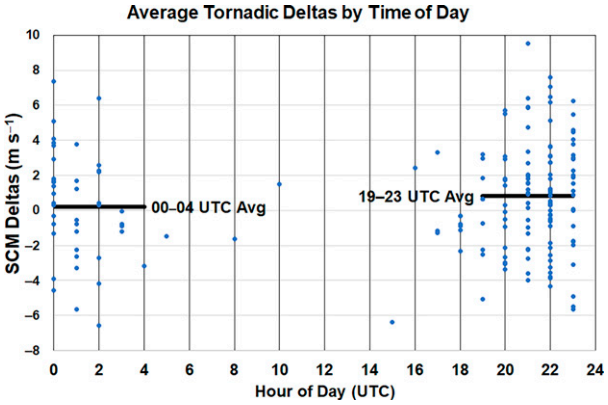

FIG. 13. Average supercell-motion deltas for all 171 cases in Tables A1 and A2 for the hour over which the deltas were computed (for the 0–6-km shear layer and 20-min storm-motion calculation). The sample size is 42 for 0000–0400 UTC and 115 for 1900–2300 UTC.

4. Conclusions and discussion

This exploratory study compared storm-motion deviations for concurrent tornadic and nontornadic supercells on a radar scan-by-scan basis. These deviations (referred to as "deltas") were defined as the shear-orthogonal distance between the observed supercell motion and the default Bunkers et al. (2000) predicted supercell motion, thus establishing a baseline for comparison. As such, deltas are zero for supercells moving precisely 7.5 m s^{-1} away from the mean wind and orthogonal to the shear vector (as defined in Bunkers et al.); larger deltas mean that supercells deviate farther away from the predicted motion (and also mean wind) in a *shear-relative sense*. Concurrent tornadic and nontornadic supercells had to occur within the same hour and generally be within the spatial proximity constraints given by Potvin et al. (2010). Model soundings from the hourly RUC or RAP were used to calculate the predicted supercell motion, and a semiautomated radar reflectivity-based tracking algorithm was used to calculate the observed supercell motion each scan. Reflectivity thresholds to define storm objects required manual adjustments in many cases in order to improve the tracking algorithm performance. A dataset of 171 cases was used for prescribing the settings pertaining to the storm-motion calculation duration and the shear layer for computing the deltas. These results were used to assess whether the deltas were superior (in tornadic versus nontornadic discrimination) compared to just using the mean absolute errors (MAEs) of the supercell-motion prediction. Next, comparisons were made between the delta time series of the tornadic versus nontornadic supercells for a variety of statistical properties (e.g., average, median, and maximum). In addition, the deltas and delta trends were compared between equal periods prior to and after tornadogenesis. Finally, the median deltas were compared to the maximum EF-scale ratings for each case, and the deltas also were examined by time of day.

These first two conclusions pertain to our methods for storm-motion duration and shear-layer depth for calculating the deltas.

- Either a 20- or 30-min duration for the storm-motion calculation is equally skillful when computing the deltas that are used to discriminate between tornadic and nontornadic supercells. However, a 20-min duration is recommended because some supercells can produce tornadoes relatively soon after convective initiation and/or supercell development. From an operational warning decision-making perspective, the 20-min duration is preferred since it provides additional lead time.
- The 0–6-km shear layer performed only slightly better than the 0–3-km layer, and modestly better than the 0–1-km layer. Overall, the 0–6-km layer is recommended, but the effective bulk wind difference layer also would be suitable (see footnote 3).

The remaining conclusions pertain to the primary results, and these results are given for the 20- and 30-min storm-motion calculations using only the 0–6-km shear layer for computing the deltas (based on the previous two bullets).

- The supercell-motion deltas resulted in the best discriminating ability between tornadic and nontornadic supercells when compared to the MAEs, with the results being much more statistically significant for the deltas versus the MAEs. The average deltas were about 1.9–2.0 m s^{-1} larger for the tornadic versus nontornadic supercells. Conversely, the MAEs were about 0.4 to 0.7 m s^{-1} *smaller* for the tornadic versus nontornadic supercells, with minimal statistical significance.
- The deltas were larger for the tornadic versus nontornadic supercells about 80% of the time. In addition, the trends in the deltas were more positive in the 15–30 min prior to tornadogenesis compared to the same time period after tornadogenesis (56%–57% of the time), and overall were positive 62%–70% of the time prior to tornadogenesis. For these same time periods, the average supercell-motion deltas were about 0.9 m s^{-1} larger after tornadogenesis compared to prior to tornadogenesis.
- The correlation between median supercell-motion deltas and maximum tornado EF-scale rating was positive and marginally statistically significant. This indicates greater

shear-relative rightward deviation as EF-scale rating increases. Otherwise, there was large variability in the delta magnitudes for each EF-scale sample (especially EF0), which contributed to a lower correlation when compared to using just the EF1–4 cases.

- The relative delta differences between tornadic and nontornadic supercells appear to be a more useful measure than the absolute magnitudes of the deltas. For 75 of the 171 total cases with negative average tornadic deltas, 70.7% of them had larger average deltas for the tornadic versus nontornadic supercells. Overall, there was near one-quartile separation in the medians after the first 15 min of the analysis hour for the tornadic versus nontornadic supercells.
- The supercell-motion deltas decreased, on average, during the early evening (≥0000 UTC) relative to the afternoon (<0000 UTC), although this difference is not statistically significant. As a result, the difference in deltas between tornadic and nontornadic supercells was greatest during the afternoon, and lesser during the evening. This possibly may be an advantage for improving warnings for the first tornado of the day (e.g., Krocak et al. 2021), especially for typical diurnal tornado events.

These results examining shear-orthogonal deviations (or deltas) are consistent with Wade et al. (2018) who found the 0–1-km SRH increased substantially in the near field of tornadic supercells (i.e., farther shear-relative rightward deviations), but the deviations were not as much for nontornadic supercells (also see Markowski et al. 1998; Parker 2014). The 1.2 m s^{-1} increase in rightward deviation (relative to the hodograph) for tornadic versus nontornadic supercells noted by Bunkers (2018) is smaller than the 1.9–2.0 m s^{-1} increase herein because, in part, that study used observed soundings that often were not as close to the supercells as were the model soundings in the present case. Coniglio and Parker (2020, their Fig. 8) showed approximately a 4 m s^{-1} difference in observed shear-orthogonal deviations between tornadic and nontornadic supercells, which may be a result of using a much higher resolution close-proximity observed sounding dataset compiled from experimental field programs. Therefore, application of the results of this study—using higher-resolution model sounding information—might provide some discrimination ability and lead time for tornadogenesis.

One advantage of using these supercell-motion deltas to distinguish between tornadic and nontornadic storms is the deltas can be calculated at far ranges (out to 230 km) from the radar. This is because the deltas rely solely on supercell-motion deviation, and calculation of supercell motion only requires reflectivity. Much of the similarly focused tornadic storms research using low-level dual-polarization data requires storms to be reasonably close to the radar, which is a substantial limitation to those studies (e.g., Van Den Broeke 2020). Even if three-dimensional reflectivity and Doppler velocity information is used in future storm-motion algorithms to identify supercell storms for the delta calculations, that still would allow radar data to be used from relatively far ranges.

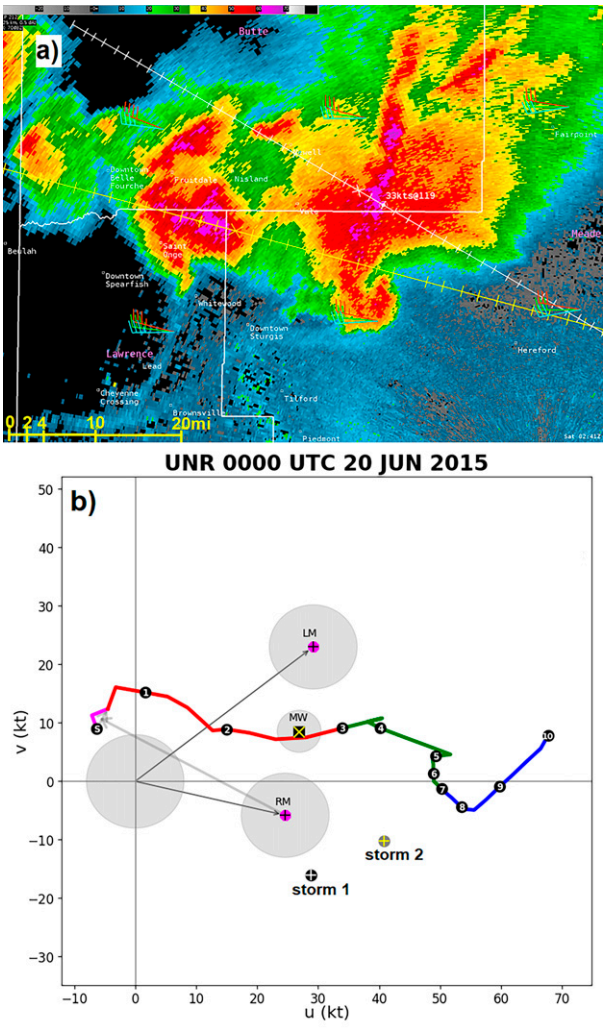

FIG. 14. (a) Rapid City, SD (KUDX), 0.5° reflectivity valid at 0241 UTC 20 Jun 2015. Green barbs represent the Bunkers et al. (2000) supercell motion (kt; 1.94 kt = 1 m s^{-1}) from the RAP model; red barbs are the same, but with a delta of +2.5 m s^{-1}; and cyan barbs are the same, but with a delta of –2.5 m s^{-1}. Storm tracks are given for the eastern supercell (white, storm 1) and western supercell (yellow, storm 2). County boundaries are white, county names are magenta, and cities are white and indicated by a small open square. The reflectivity legend (dBZ) is given at top left. (b) The 0–10-km hodograph (kt) for Rapid City, SD (UNR), valid at 0000 UTC 20 Jun 2015. The predicted right-moving and left-moving supercell motions are plotted as magenta circles/black plus signs, and the observed motions for storm 1 and storm 2 are plotted as a black circle/white plus sign and gray circle/yellow plus sign, respectively. Storm 1 (which was tornadic from 0257 to 0326 UTC) has a larger delta than storm 2.

Using these supercell-motion deltas to assess tornado potential is just one part of the multifaceted tornado-warning decision-making process. There are many factors operational forecasters rely on to decide whether or not to issue a tornado warning for a given storm—including information from the

TABLE A1. Cases from Van Den Broeke (2020) used for this study. Radar site identification information is listed at https://www.roc.noaa.gov/WSR88D/Program/NetworkSites.aspx. The year, month, day, and hour information corresponds to the UTC time of the RAP/RUC proximity sounding; cenlat and cenlon refer to the latitude and longitude of the sounding, respectively; EF time refers to the EF-scale rating and start time of the supercell's first tornado (obtained from https://www.ncdc.noaa.gov/stormevents/); and REF1 and REF2 represent the outer and inner reflectivity thresholds for storm tracking, respectively (see Fig. 4). The first 31 rows were derived from Van Den Broeke's Table 1, and the last three rows were derived from his Table 2 (34 cases total).

Radar	Year	Month	Day	Hour (UTC)	Cenlat (°)	Cenlon (°)	EF time (UTC)	REF1	REF2
KOHX	2012	4	26	2300	35.4915	−86.5816	EF0 2400	35	42
KDDC	2012	4	30	2200	37.8075	−99.7316	EF0 2252	47	52
KEWX	2012	5	10	1800	28.109	−98.148	EF0 1846	45	50
KMQT	2012	6	9	0000	46.411	−87.859	EF1 0013	28	40
KFFC	2013	3	18	2200	33.1985	−83.7059	EF2 2210	49	54
KINX	2013	3	31	0200	35.5645	−95.0139	EF0 0235	48	53
KSRX	2013	3	31	0400	35.04	−94.6403	EF1 0420	45	50
KFDR	2013	4	17	2300	34.2158	−98.3941	EF0 2350	45	50
KFWS	2013	5	15	2300	32.433	−97.7014	EF0 2341	45	50
KDDC	2013	5	19	0000	37.9397	−98.9023	EF4 0018	45	50
KTLX	2013	5	19	2100	35.4079	−97.1006	EF1 2122	35	42
KTLX	2013	5	19	2200	34.8231	−97.1425	EF3 2300	38	43
KINX	2013	5	20	2000	35.9602	−95.9727	EF1 2051	45	50
KEAX	2013	5	20	2100	38.4978	−93.7906	EF1 2157	45	50
KINX	2013	5	30	2300	35.7215	−95.8739	EF0 2349	45	50
KRAX	2013	6	18	2200	35.6957	−78.2978	EF0 2230	35	42
KLBB	2013	6	19	2200	33.2791	−102.202	EF2 2232	50	55
KDTX	2013	8	28	0300	42.3307	−84.1544	EF0 0354	40	45
KBIS	2013	8	31	0000	46.5265	−101.048	EF0 0010	43	48
KUEX	2014	5	11	2000	40.0001	−98.0097	EF0 2026	45	50
KDVN	2015	4	9	2200	41.2091	−90.6515	EF1 2204	45	50
KFWS	2015	4	27	0200	31.797	−97.5643	EF0 0209	45	50
KFDR	2015	5	8	2100	33.9868	−99.0581	EF0 2122	45	50
KTLX	2015	5	19	1900	34.49	−97.4137	EF0 1940	40	45
KDDC	2015	5	27	2000	37.9511	−100.181	EF0 2003	45	50
KFTG	2015	6	4	2200	39.1837	−103.326	EF0 2238	35	40
KEAX	2015	9	18	2300	38.287	−93.9676	EF1 2309	42	47
KDGX	2016	2	2	2000	32.1908	−88.9733	EF1 2048	48	53
KRAX	2016	2	24	2000	35.7487	−79.1154	EF1 2100	42	49
KFDR	2016	4	29	2000	34.6182	−98.0279	EF1 2029	47	52
KFDR	2017	10	21	2200	34.1541	−98.5189	EFU 2223	43	48
KTLX	2013	5	30	2200	34.1807	−97.3503	EF0 2258	40	45
KMPX	2013	8	6	2200	45.655	−94.4575	EF0 2217	45	50
KDIX	2013	8	13	1000	39.6089	−75.4764	EF0 1001	45	50

radar, storm spotters, satellite, lightning, and environment. For example, both the mesoscale environment and dual-polarization signatures have received emphasis in recent years (e.g., Loeffler et al. 2020). Accordingly, the supercell-motion deltas may be just one tool among many that may, in certain situations, help the warning forecaster tip the scale in favor of, or against, a tornado warning (and possibly in drawing warning polygons).

One limitation of this exploratory study is that only concurrent pairs of tornadic and nontornadic supercells were tested (using a single sounding). However, there are days when long-lived isolated supercells (Bunkers et al. 2006) may occur and the deltas would only be applicable in an absolute sense (i.e., no comparison would be possible between nearby storms). Applying the deltas in these situations would require a real-time calibration based on the occurrence/nonoccurrence of tornadoes. In this way, a minimum delta range conceivably could be determined for that event. This is left for future study.

This exploratory analysis of supercell-motion deltas supports further investigation, such as in applied experiments through the Hazardous Weather Testbed (HWT; Calhoun et al. 2021) using advanced tools such as the ProbSevere real-time probabilistic warning guidance system (Cintineo et al. 2020). The HWT provides an avenue for forecasters and researchers to work collaboratively in an effort to test and improve on new technologies that may be applied to severe convective storms forecasting and warning activities. ProbSevere has a component to predict the probability of a tornado (ProbTor) in the subsequent 60 min; this relies on environmental, satellite, lightning, and radar information, and is among many experimental cutting-edge technologies that have been tested at the HWT. ProbSevere also uses a proven, fully automated operational tracking algorithm.

TABLE A2. As in Table A1, but for 137 cases developed herein using the methods outlined in section 2a. The KGLD/KLNX case from 17 May 2019 used the KGLD radar for the tornadic supercell and the KLNX radar for the nontornadic supercell. The 80 cases below the blank row were gathered based on their significance, our awareness of them, and/or their documentation in the literature.

Radar	Year	Month	Day	Hour (UTC)	Cenlat (°)	Cenlon (°)	EF time (UTC)	REF1	REF2
KTLX	2017	3	27	0000	35.3074	−95.7625	EF0 0018	45	50
KLBB	2017	5	10	0000	33.2382	−102.829	EFU 0046	43	48
KLBB	2017	5	10	0100	33.5994	−102.613	EFU 0145	45	50
KLBB	2017	5	10	0200	33.1297	−103.37	EFU 0231	40	45
KFDR	2017	5	16	2100	34.9688	−100.223	EF0 2139	45	50
KFDR	2017	5	16	2200	34.547	−99.9803	EF1 2216	43	48
KFDR	2017	5	16	2300	34.8502	−99.4173	EFU 2308	45	50
KFDR	2017	5	18	1900	34.4506	−99.2634	EF0 1902	45	50
KFDR	2017	5	18	2000	34.7325	−98.8966	EF1 2029	42	47
KFDR	2017	5	18	2100	35.0781	−98.5145	EF0 2133	45	50
KCYS	2017	6	12	2200	41.2182	−104.007	EF1 2240	45	50
KCYS	2017	6	13	0000	41.652	−103.19	EF1 0001	40	45
KUEX	2018	5	1	2100	40.5888	−97.9129	EF0 2135	45	50
KFDR	2018	5	2	2100	34.5981	−99.118	EF0 2125	45	50
KFDR	2018	5	2	2200	34.2959	−98.7659	EFU 2246	45	50
KFDR	2018	5	2	2300	34.4256	−98.367	EFU 2310	45	50
KDDC	2018	5	29	2100	37.6866	−99.8444	EF0 2144	40	45
KFTG	2018	6	19	2000	40.1452	−104.261	EF0 2016	45	50
KFTG	2018	6	19	2200	39.288	−103.355	EF0 2248	48	53
KUEX	2018	6	19	2200	40.1475	−98.9249	EF0 2242	45	50
KUEX	2018	6	30	2000	40.343	−98.8733	EF0 2040	45	50
KCYS	2018	7	29	1900	41.5617	−105.024	EF0 1955	45	50
KCYS	2018	7	29	2000	41.1778	−104.741	EF0 2045	45	50
KCYS	2018	7	29	2200	40.297	−104.004	EF2 2231	52	57
KMXX	2019	3	3	2000	32.2235	−84.6575	EF1 2000	45	50
KLSX	2019	3	24	2100	37.6305	−91.3278	EF0 2131	45	50
KAMA	2019	5	7	2000	35.3768	−101.575	EFU 2127	45	50
KGLD/KLNX	2019	5	17	2200	40.5497	−101.3677	EF0 0136	45	50
KDDC	2019	5	18	0100	37.6958	−99.7828	EF0 0136	45	50
KDDC	2019	5	18	0200	38.074	−99.3471	EF2 0230	45	50
KFDR	2019	5	20	2200	34.3449	−99.9668	EF2 2212	45	50
KMAF	2019	5	20	2300	32.272	−101.927	EF2 2352	45	50
KTLX	2019	5	22	2100	35.222	−96.0295	EF1 2129	42	47
KIWX	2019	5	27	2300	40.659	−87.0269	EF3 2351	45	50
KILN	2019	5	28	0200	39.5844	−84.2893	EF4 0241	45	50
KILN	2019	5	28	0300	39.4458	−83.7028	EF4 0300	45	50
KPBZ	2019	5	28	1900	41.1065	−79.1395	EF0 1945	43	48
KBGM	2019	5	28	2000	41.6796	−77.3716	EF1 2050	39	44
KUEX	2019	5	28	2200	39.1218	−98.4062	EF2 2220	45	50
KLWX	2019	5	30	1800	39.1535	−77.5974	EF0 1848	39	44
KFWS	2020	3	19	0100	32.7525	−98.8157	EF0 0156	42	47
KGWX	2020	3	24	2200	34.3108	−88.1737	EF1 2227	42	47
KNQA	2020	4	9	0000	35.7752	−90.217	EF0 0047	45	50
KDGX	2020	4	12	2000	30.7775	−90.17	EF4 2039	40	45
KGSP	2020	5	5	2200	34.5825	−82.1744	EF1 2232	40	45
KEWX	2020	5	12	1500	29.641	−96.9148	EF0 1554	38	43
KSRX	2020	5	23	0200	34.8109	−94.795	EF1 0259	43	48
KDVN	2020	5	23	1700	42.0778	−91.2326	EF0 1730	40	45
KDVN	2020	5	23	1900	41.7214	−89.3145	EF1 1929	40	45
KILX	2020	5	23	1800	40.8125	−88.7362	EF0 1854	43	48
KLBB	2020	5	23	2200	33.1686	−100.801	EFU 2214	45	50
KMVX	2020	6	8	2100	47.3534	−97.5148	EF0 2117	40	45
KLSX	2020	6	27	2200	37.814	−91.8158	EF0 2243	41	46
KARX	2020	6	29	0100	44.3477	−91.3243	EF0 0137	42	47
KFCX	2020	8	1	2200	37.3483	−81.0624	EF0 2225	37	42
KLNX	2020	8	14	0000	41.9982	−100.46	EF0 0025	45	50
KMPX	2020	8	14	2200	44.6404	−93.8219	EF0 2245	45	50

TABLE A2. (*Continued*)

Radar	Year	Month	Day	Hour (UTC)	Cenlat (°)	Cenlon (°)	EF time (UTC)	REF1	REF2
—	—	—	—	—	—	—	—	—	—
KTWX	2008	5	28	2100	39.1961	−95.7420	EF3 2116	45	50
KUEX	2008	5	30	0100	39.4694	−98.0367	EF0 0116	40	45
KTLX	2009	2	10	2000	35.0655	−97.3788	EF1 2036	45	50
KTLX	2009	2	10	2100	35.0661	−97.4513	EF1 2124	45	50
KCYS	2009	6	5	2200	41.3188	−103.957	EF2 2207	45	50
KUDX	2009	7	13	2300	43.7032	−101.742	EF0 2335	45	50
KUDX	2009	7	14	0000	44.5129	−103.567	EF2 0010	45	50
KFTG	2010	6	11	0000	39.6611	−103.714	EF0 0052	42	52
KOAX	2011	4	10	0000	41.8232	−96.2662	EF3 0020	47	52
KTLX	2011	4	14	2300	34.2049	−95.8312	EF1 2303	47	52
KBMX	2011	4	27	2100	33.3349	−88.5131	EF2 2143	43	48
KSGF	2011	5	22	2200	36.8541	−94.1515	EF2 2234	45	50
KFWS	2012	4	3	1800	32.1469	−96.6656	EF2 1808	39	44
KDDC	2013	4	7	2300	38.8294	−98.7212	EF0 2338	45	50
KILX	2013	11	17	1700	39.5568	−89.3901	EF0 1730	40	45
KCYS	2014	5	20	2300	41.597	−103.612	EF0 2325	45	50
KOAX	2014	6	16	2100	42.1973	−96.1896	EF4 2100	43	48
KOAX	2014	6	16	2200	42.0183	−95.6675	EF0 2241	43	48
KBIS	2014	6	17	0200	46.3834	−102.0030	EF0 0223	40	45
KFSD	2014	6	18	0300	43.2671	−96.8525	EF2 0344	40	45
KMVX	2014	9	4	0800	46.2815	−98.0719	EF0 0826	45	50
KUDX	2015	6	20	0200	44.156	−103.111	EF2 0257	45	50
KDGX	2016	2	15	1800	31.2314	−90.239	EF2 1810	45	50
KLCH	2016	2	15	1900	29.8416	−92.1858	EF0 1904	40	45
KEVX	2016	2	15	2100	30.8422	−86.9529	EF3 2132	43	48
KSRX	2016	3	13	2000	34.5771	−93.9357	EF1 2056	40	45
KLZK	2016	3	13	2100	34.6793	−93.4629	EF1 2148	45	50
KLZK	2016	3	13	2300	35.3111	−92.1175	EF0 2315	43	48
KILX	2016	3	15	2300	40.0575	−90.4022	EF2 2326	46	51
KNQA	2016	3	27	2200	35.8214	−-88.8359	EF1 2224	38	43
KINX	2016	3	31	0000	36.5962	−95.4613	EF1 0013	45	50
KAMA	2016	4	16	0000	36.0606	−102.1173	EF0 0050	41	48
KLBB	2016	4	16	2100	33.1965	−100.3271	EF0 2155	45	50
KLBB	2016	4	16	2200	33.0183	−100.4768	EF0 2250	43	48
KVWX	2016	4	27	2300	39.0385	−88.4062	EF0 2358	43	48
KIND	2016	4	28	1900	39.7620	−86.1643	EF1 1926	37	42
KLBB	2016	4	28	2200	33.8930	−100.7625	EF0 2240	45	50
KIND	2016	5	2	0000	40.0374	−86.5572	EF0 0038	45	50
KHPX	2016	5	10	2200	37.1744	−86.6764	EF1 2225	40	45
KPAH	2016	5	10	2200	37.2267	−88.062	EF0 2256	38	43
KAMA	2016	5	16	2100	36.1576	−102.95	EF0 2139	42	47
KMAF	2016	5	22	2300	32.6291	−100.7954	EF3 2313	45	50
KVNX	2016	5	24	0100	36.0509	−99.4808	EF0 0125	40	45
KAMA	2016	5	24	0200	34.7459	−100.3522	EFU 0230	45	50
KMQT	2016	5	24	1800	46.0095	−88.0922	EF1 1821	38	43
KDDC	2016	5	24	2200	37.0856	−99.9145	EF3 2255	45	50
KICT	2016	5	26	0300	38.5729	−96.0161	EF1 0325	45	50
KEAX	2016	5	26	2100	39.0644	−93.5974	EF0 2203	45	50
KEWX	2016	5	29	0000	30.0133	−99.1137	EF2 0050	45	50
KDYX	2016	5	30	0100	32.9763	−99.4821	EF0 0109	45	50
KLWX	2016	6	16	1900	39.6543	−79.0837	EF0 1935	40	45
KLNX	2016	6	27	2200	40.5713	−102.3208	EF0 2240	45	50
KGLD	2016	6	27	2300	40.2352	−102.0807	EF0 2330	45	50
KLNX	2016	7	6	2100	42.0071	−102.3969	EF0 2114	40	45
KLNX	2016	7	6	2200	42.0086	−102.031	EF0 2256	45	50
KLNX	2016	7	6	2300	42.0133	−101.2802	EF1 2325	35	40
KGLD	2016	7	15	2100	38.1214	−101.4236	EF1 2148	45	50
KLOT	2016	7	18	0100	40.7435	−89.0311	EF0 0118	40	45

TABLE A2. (*Continued*)

Radar	Year	Month	Day	Hour (UTC)	Cenlat (°)	Cenlon (°)	EF time (UTC)	REF1	REF2
KGYX	2016	7	18	1600	44.7076	−71.6799	EF0 1642	45	50
KCYS	2016	7	29	2300	41.1747	−103.7929	EF0 2322	45	50
KMVX	2016	8	27	2100	48.1535	−96.768	EF0 2112	45	50
KMVX	2016	8	27	2300	47.0888	−97.0659	EF3 2302	43	48
KGLD	2016	9	2	2200	40.4050	−102.129	EF0 2205	43	48
KFDX	2016	9	15	2000	33.1164	−104.4142	EF0 2010	45	50
KCCX	2016	9	17	2200	41.4371	−79.3698	EF1 2235	43	48
KMAF	2016	9	18	0000	32.0184	−103.4418	EF1 0013	45	50
KICT	2016	10	6	1900	37.2613	−96.3719	EF0 1926	43	48
KDGX	2016	11	29	2100	32.0329	−89.7288	EF1 2157	41	46
KDGX	2016	11	29	2300	32.4071	−89.6684	EF1 2349	43	48
KNQA	2016	11	30	0000	33.8103	−87.9744	EF1 0012	43	48
KGWX	2016	11	30	0100	32.9170	−88.333	EF1 0115	45	50
KDDC	2017	10	6	2300	37.8519	−99.1909	EF0 2356	45	50
KOHX	2018	2	24	2100	36.7737	−86.4126	EF1 2153	45	50
KICT	2018	5	14	2300	37.5403	−96.4874	EF0 2335	45	50
KFWS	2019	10	21	0100	32.5617	−98.6759	EF3 0158	45	50
KLCH	2019	12	16	1700	30.4954	−93.1223	EF3 1710	42	47
KOHX	2020	3	3	0500	35.7451	−87.9889	EF2 0505	45	50
KFDR	2021	4	23	2200	34.087	−99.3773	EFU 2243	42	47
KFDR	2021	4	23	2300	34.0518	−98.9762	EFU 2310	45	50
KSJT	2021	5	18	0000	31.7744	−100.837	EFU 0011	45	50

Testing the supercell deviant-motion concepts in a pseudo-operational testbed environment to provide forecaster assessment and feedback could help refine the algorithm (including storm tracking as noted in section 3a) and offer options in which the delta fields could be effectively displayed in operations.

In the absence of immediate testing and/or a consistent display of the deltas at this time, various meteorological software packages can plot the Bunkers et al. (2000) right-moving supercell motion using the standard 7.5 m s^{-1} distance from the mean wind (delta = 0 m s^{-1} in this case); for example, see the SPC observed sounding web page at https://www.spc.noaa.gov/exper/soundings/. Then, for reference, additional supercell-motion vectors can be plotted for smaller (e.g., 5.0 m s^{-1}) and larger (e.g., 10.0 m s^{-1}) distances from the mean wind (e.g., Fig. 14; equating to deltas of −2.5 and +2.5 m s^{-1}, respectively). Displays such as Fig. 14a (with the three supercell-motion predictions: cyan, green, and red), when combined with real-time radar data, can be used to provide situation awareness (Endsley 1995) of supercell motions deviating more or less than the baseline prediction. This might prove helpful, at times, in the tornado-warning decision-making process.

Acknowledgments. We thank Dave Hintz (meteorologist-in-charge, NWS, Rapid City, SD) for supporting this work, Dr. Keith Sherburn (NWS Rapid City) for an early review of the manuscript, Steve Weiss (retired, SPC) for an exceptionally incisive and thorough pre-review of the manuscript, Jeff Manion (NWS Central Region) for a technical evaluation prior to submitting the manuscript for formal review, the Statistical Cross-Disciplinary Collaboration and Consulting Lab at UNL for statistical advice, Dr. Matthew Flournoy (CIMMS) for advice on Figs. 9 and 12, and Roger Edwards (SPC) and two anonymous reviewers for several excellent suggestions for improvement and clarification.

Data availability statement. All RUC and RAP model output used in this study were obtained from the NOAA Operational Model Archive and Distribution System (NOMADS) archive (https://www.ncei.noaa.gov/thredds/model/model.html). The Python code used for the analysis herein is available online in the GitHub repository at https://github.com/mwilson14/StormMotionDeltas. Data files for the 171 cases and corresponding tornado reports are available in comma-separated values (CSV) format upon request; these were used as input into the Python programs.

APPENDIX

Supercell Cases Used in This Study

The proof-of-concept dataset (Table A1) and additional supercell cases (Table A2) are listed here. Both datasets were combined for a total of 171 cases used in the analysis.

REFERENCES

Anderson-Frey, A. K., Y. P. Richardson, A. R. Dean, R. L. Thompson, and B. T. Smith, 2016: Investigation of near-storm environments for tornado events and warnings. *Wea. Forecasting*, **31**, 1771–1790, https://doi.org/10.1175/WAF-D-16-0046.1.

Benjamin, S. G., and Coauthors, 2004: An hourly assimilation–forecast cycle: The RUC. *Mon. Wea. Rev.*, **132**, 495–518, https://doi.org/10.1175/1520-0493(2004)132<0495:AHACTR>2.0.CO;2.

——, and Coauthors, 2016: A North American hourly assimilation and model forecast cycle: The Rapid Refresh. *Mon. Wea. Rev.*, **144**, 1669–1694, https://doi.org/10.1175/MWR-D-15-0242.1.

Bluestein, H. B., D. T. Lindsey, D. Bikos, D. W. Reif, and Z. B. Wienhoff, 2019: The relationship between overshooting tops in a tornadic supercell and its radar-observed evolution. *Mon. Wea. Rev.*, **147**, 4151–4176, https://doi.org/10.1175/MWR-D-19-0159.1.

Brooks, H. E., and J. Correia Jr., 2018: Long-term performance metrics for National Weather Service tornado warnings. *Wea. Forecasting*, **33**, 1501–1511, https://doi.org/10.1175/WAF-D-18-0120.1.

——, C. A. Doswell III, and J. Cooper, 1994: On the environments of tornadic and nontornadic mesocyclones. *Wea. Forecasting*, **9**, 606–618, https://doi.org/10.1175/1520-0434(1994)009<0606:OTEOTA>2.0.CO;2.

Browning, K. A., 1965: The evolution of tornadic storms. *J. Atmos. Sci.*, **22**, 664–668, https://doi.org/10.1175/1520-0469(1965)022<0664:TEOTS>2.0.CO;2.

——, and G. B. Foote, 1976: Airflow and hail growth in supercell storms and some implications for hail suppression. *Quart. J. Roy. Meteor. Soc.*, **102**, 499–533, https://doi.org/10.1002/qj.49710243303.

Bunkers, M. J., 2018: Observations of right-moving supercell motion forecast errors. *Wea. Forecasting*, **33**, 145–159, https://doi.org/10.1175/WAF-D-17-0133.1.

——, B. A. Klimowski, J. W. Zeitler, R. L. Thompson, and M. L. Weisman, 2000: Predicting supercell motion using a new hodograph technique. *Wea. Forecasting*, **15**, 61–79, https://doi.org/10.1175/1520-0434(2000)015<0061:PSMUAN>2.0.CO;2.

——, M. R. Hjelmfelt, and P. L. Smith, 2006: An observational examination of long-lived supercells. Part I: Characteristics, evolution, and demise. *Wea. Forecasting*, **21**, 673–688, https://doi.org/10.1175/WAF949.1.

——, D. A. Barber, R. L. Thompson, R. Edwards, and J. Garner, 2014: Choosing a universal mean wind for supercell motion prediction. *J. Oper. Meteor.*, **2**, 115–129, https://doi.org/10.15191/nwajom.2014.0211.

Calhoun, K. M., K. L. Berry, D. M. Kingfield, T. Meyer, M. J. Krocak, T. M. Smith, G. Stumpf, and A. Gerard, 2021: The experimental warning program of NOAA's Hazardous Weather Testbed. *Bull. Amer. Meteor. Soc.*, **102**, E2229–E2246, https://doi.org/10.1175/BAMS-D-21-0017.1.

Chrisman, J. N., 2011: Supplemental adaptive intra-volume low-level scan (SAILS). ROC Engineering, NOAA, 13 pp., https://www.roc.noaa.gov/wsr88d/PublicDocs/NewTechnology/SAILS_Initial_Presentation_Sep_2011.pdf.

——, 2014: Multiple elevation scan option for SAILS (MESO-SAILS): The next step in dynamic scanning for the WSR-88D. NOAA, 27 pp., https://www.roc.noaa.gov/wsr88d/PublicDocs/NewTechnology/MESO-SAILS_Description_Briefing_Jan_2014.pdf.

Cintineo, J. L., M. J. Pavolonis, J. M. Sieglaff, L. Cronce, and J. Brunner, 2020: NOAA ProbSevere v2.0—ProbHail, ProbWind, and ProbTor. *Wea. Forecasting*, **35**, 1523–1543, https://doi.org/10.1175/WAF-D-19-0242.1.

Coffer, B. E., and M. D. Parker, 2017: Simulated supercells in nontornadic and tornadic VORTEX2 environments. *Mon. Wea. Rev.*, **145**, 149–180, https://doi.org/10.1175/MWR-D-16-0226.1.

——, ——, R. L. Thompson, B. T. Smith, and R. E. Jewell, 2019: Using near-ground storm relative helicity in supercell tornado forecasting. *Wea. Forecasting*, **34**, 1417–1435, https://doi.org/10.1175/WAF-D-19-0115.1.

Coniglio, M. C., and M. D. Parker, 2020: Insights into supercells and their environments from three decades of targeted radiosonde observations. *Mon. Wea. Rev.*, **148**, 4893–4915, https://doi.org/10.1175/MWR-D-20-0105.1.

Davies, J., 1990: Midget supercell spawns tornadoes. *Weatherwise*, **43**, 260–261, https://doi.org/10.1080/00431672.1990.9929350.

Doswell, C. A., III, 2007: Small sample size and data quality issues illustrated using tornado occurrence data. *Electron. J. Severe Storms Meteor.*, **2** (5), https://ejssm.org/archives/2007/vol-2-5-2007/.

——, and D. W. Burgess, 1988: On some issues of United States tornado climatology. *Mon. Wea. Rev.*, **116**, 495–501, https://doi.org/10.1175/1520-0493(1988)116<0495:OSIOUS>2.0.CO;2.

Edwards, R., A. R. Dean, R. L. Thompson, and B. T. Smith, 2012: Convective modes for significant severe thunderstorms in the contiguous United States. Part III: Tropical cyclone tornadoes. *Wea. Forecasting*, **27**, 1507–1519, https://doi.org/10.1175/WAF-D-11-00117.1.

——, J. G. LaDue, J. T. Ferree, K. Scharfenberg, C. Maier, and W. L. Coulbourne, 2013: Tornado intensity estimation: Past, present, and future. *Bull. Amer. Meteor. Soc.*, **94**, 641–653, https://doi.org/10.1175/BAMS-D-11-00006.1.

——, H. E. Brooks, and H. Cohn, 2021: Changes in tornado climatology accompanying the enhanced Fujita scale. *J. Appl. Meteor. Climatol.*, **60**, 1465–1482, https://doi.org/10.1175/JAMC-D-21-0058.1.

Endsley, M. R., 1995: Toward a theory of situation awareness in dynamic systems. *J. Hum. Factors Ergon. Soc.*, **37**, 32–64, https://doi.org/10.1518/001872095779049543.

Fankhauser, J. C., 1971: Thunderstorm-environment interactions determined from aircraft and radar observations. *Mon. Wea. Rev.*, **99**, 171–192, https://doi.org/10.1175/1520-0493(1971)099<0171:TIDFAA>2.3.CO;2.

Flournoy, M. D., M. C. Coniglio, and E. N. Rasmussen, 2021: Examining relationships between environmental conditions and supercell motion in time. *Wea. Forecasting*, **36**, 737–755, https://doi.org/10.1175/WAF-D-20-0192.1.

Hales, J. E., Jr., 1988: Improving the watch/warning program through use of significant event data. Preprints, *15th Conf. on Severe Local Storms*, Baltimore, MD, Amer. Meteor. Soc., 165–168.

Helmus, J. J., and S. M. Collis, 2016: The Python ARM Radar Toolkit (Py-ART), a library for working with weather radar data in the Python programming language. *J. Open Res. Software*, **4**, e25, https://doi.org/10.5334/jors.119.

Johnson, J. T., P. L. MacKeen, A. Witt, E. D. Mitchell, G. J. Stumpf, M. D. Eilts, and K. W. Thomas, 1998: The storm cell identification and tracking algorithm: An enhanced WSR-88D algorithm. *Wea. Forecasting*, **13**, 263–276, https://doi.org/10.1175/1520-0434(1998)013<0263:TSCIAT>2.0.CO;2.

Jones, T. A., K. M. McGrath, and J. T. Snow, 2004: Association between NSSL mesocyclone detection algorithm-detected vortices and tornadoes. *Wea. Forecasting*, **19**, 872–890, https://doi.org/10.1175/1520-0434(2004)019<0872:ABNMDA>2.0.CO;2.

Klees, A. M., Y. P. Richardson, P. M. Markowski, C. Weiss, J. M. Wurman, and K. K. Kosiba, 2016: Comparison of the tornadic and nontornadic supercells intercepted by VORTEX2 on 10 June 2010. *Mon. Wea. Rev.*, **144**, 3201–3231, https://doi.org/10.1175/MWR-D-15-0345.1.

Klimowski, B. A., and M. J. Bunkers, 2002: Comments on "Satellite Observations of a Severe Supercell Thunderstorm on 24 July 2000 Made during the GOES-11 Science Test." *Wea. Forecasting*, **17**, 1111–1117, https://doi.org/10.1175/1520-0434(2002)017<1111:COSOOA>2.0.CO;2.

Krocak, M. J., M. D. Flournoy, and H. E. Brooks, 2021: Examining sub-daily tornado warning performance and associated environmental characteristics. *Wea. Forecasting*, **36**, 1779–1784, https://doi.org/10.1175/WAF-D-21-0097.1.

Loeffler, S. D., M. R. Kumjian, M. Jurewicz, and M. M. French, 2020: Differentiating between tornadic and nontornadic supercells using polarimetric radar signatures of hydrometeor size sorting. *Geophys. Res. Lett.*, **47**, e2020GL088242, https://doi.org/10.1029/2020GL088242.

Markowski, P., and Y. Richardson, 2009: Tornadogenesis: Our current understanding, forecasting considerations, and questions to guide future research. *Atmos. Res.*, **93**, 3–10, https://doi.org/10.1016/j.atmosres.2008.09.015.

——, and ——, 2010: *Mesoscale Meteorology in Midlatitudes.* John Wiley & Sons, 432 pp.

——, J. M. Straka, E. N. Rasmussen, and D. O. Blanchard, 1998: Variability of storm-relative helicity during VORTEX. *Mon. Wea. Rev.*, **126**, 2959–2971, https://doi.org/10.1175/1520-0493(1998)126<2959:VOSRHD>2.0.CO;2.

——, ——, and ——, 2002: Direct surface thermodynamic observations within the rear-flank downdrafts of nontornadic and tornadic supercells. *Mon. Wea. Rev.*, **130**, 1692–1721, https://doi.org/10.1175/1520-0493(2002)130<1692:DSTOWT>2.0.CO;2.

——, C. Hannon, J. Frame, E. Lancaster, A. Pietrycha, R. Edwards, and R. L. Thompson, 2003: Characteristics of vertical wind profiles near supercells obtained from the rapid update cycle. *Wea. Forecasting*, **18**, 1262–1272, https://doi.org/10.1175/1520-0434(2003)018<1262:COVWPN>2.0.CO;2.

——, M. Majcen, Y. Richardson, J. Marquis, and J. Wurman, 2011: Characteristics of the wind field in three nontornadic low-level mesocyclones observed by the Doppler on wheels radars. *Electron. J. Severe Storms Meteor.*, **6** (3), https://ejssm.org/archives/2011/vol-6-3-2011/.

Milton, J. S., and J. C. Arnold, 1990: *Introduction to Probability and Statistics: Principles and Applications for Engineering and the Computing Sciences.* McGraw-Hill, 700 pp.

Moller, A. R., C. A. Doswell III, M. P. Foster, and G. R. Woodall, 1994: The operational recognition of supercell thunderstorm environments and storm structures. *Wea. Forecasting*, **9**, 327–347, https://doi.org/10.1175/1520-0434(1994)009<0327:TOROST>2.0.CO;2.

NOAA, 2011: NWS Central Region service assessment: Joplin, Missouri, tornado—May 22, 2011. U.S. Dept. of Commerce, NOAA/NWS, Central Region Headquarters, Kansas City, MO, 41 pp., https://www.weather.gov/media/publications/assessments/Joplin_tornado.pdf.

Nowotarski, C. J., P. M. Markowski, and Y. P. Richardson, 2011: The characteristics of numerically simulated supercell storms situated over statically stable boundary layers. *Mon. Wea. Rev.*, **139**, 3139–3162, https://doi.org/10.1175/MWR-D-10-05087.1.

Parish, T. R., 2017: On the forcing of the summertime Great Plains low-level jet. *J. Atmos. Sci.*, **74**, 3937–3953, https://doi.org/10.1175/JAS-D-17-0059.1.

Parker, M. D., 2014: Composite VORTEX2 supercell environments from near-storm soundings. *Mon. Wea. Rev.*, **142**, 508–529, https://doi.org/10.1175/MWR-D-13-00167.1.

Peters, J. M., C. J. Nowotarski, J. P. Mulholland, and R. L. Thompson, 2020: The influences of effective inflow layer streamwise vorticity and storm-relative flow on supercell updraft properties. *J. Atmos. Sci.*, **77**, 3033–3057, https://doi.org/10.1175/JAS-D-19-0355.1.

Potvin, C. K., K. L. Elmore, and S. J. Weiss, 2010: Assessing the impacts of proximity sounding criteria on the climatology of significant tornado environments. *Wea. Forecasting*, **25**, 921–930, https://doi.org/10.1175/2010WAF2222368.1.

Ramsay, H. A., and C. A. Doswell III, 2005: A sensitivity study of hodograph-based methods for estimating supercell motion. *Wea. Forecasting*, **20**, 954–970, https://doi.org/10.1175/WAF889.1.

Rasmussen, E. N., and D. O. Blanchard, 1998: A baseline climatology of sounding-derived supercell and tornado forecast parameters. *Wea. Forecasting*, **13**, 1148–1164, https://doi.org/10.1175/1520-0434(1998)013<1148:ABCOSD>2.0.CO;2.

Shapiro, A., E. Fedorovich, and S. Rahimi, 2016: A unified theory for the Great Plains low-level jet. *J. Atmos. Sci.*, **73**, 3037–3057, https://doi.org/10.1175/JAS-D-15-0307.1.

Stumpf, G. J., A. Witt, E. D. Mitchell, P. L. Spencer, J. T. Johnson, M. D. Eilts, K. W. Thomas, and D. W. Burgess, 1998: The National Severe Storms Laboratory mesocyclone detection algorithm for the WSR-88D. *Wea. Forecasting*, **13**, 304–326, https://doi.org/10.1175/1520-0434(1998)013<0304:TNSSLM>2.0.CO;2.

Thompson, R. L., R. Edwards, J. A. Hart, K. L. Elmore, and P. Markowski, 2003: Close proximity soundings within supercell environments obtained from the Rapid Update Cycle. *Wea. Forecasting*, **18**, 1243–1261, https://doi.org/10.1175/1520-0434(2003)018<1243:CPSWSE>2.0.CO;2.

——, C. M. Mead, and R. Edwards, 2007: Effective storm-relative helicity and bulk shear in supercell thunderstorm environments. *Wea. Forecasting*, **22**, 102–115, https://doi.org/10.1175/WAF969.1.

——, B. T. Smith, J. S. Grams, A. R. Dean, and C. Broyles, 2012: Convective modes for significant severe thunderstorms in the contiguous United States. Part II: Supercell and QLCS tornado environments. *Wea. Forecasting*, **27**, 1136–1154, https://doi.org/10.1175/WAF-D-11-00116.1.

Trapp, R. J., G. J. Stumpf, and K. L. Manross, 2005: A reassessment of the percentage of tornadic mesocyclones. *Wea. Forecasting*, **20**, 680–687, https://doi.org/10.1175/WAF864.1.

Van Den Broeke, M. S., 2020: A preliminary polarimetric radar comparison of pretornadic and nontornadic supercell storms. *Mon. Wea. Rev.*, **148**, 1567–1584, https://doi.org/10.1175/MWR-D-19-0296.1.

Wade, A. R., M. C. Coniglio, and C. L. Ziegler, 2018: Comparison of near- and far-field supercell inflow environments using radiosonde observations. *Mon. Wea. Rev.*, **146**, 2403–2415, https://doi.org/10.1175/MWR-D-17-0276.1.

Wakimoto, R. M., H. Cai, and H. V. Murphey, 2004: The Superior, Nebraska, supercell during BAMEX. *Bull. Amer.*

Meteor. Soc., **85**, 1095–1106, https://doi.org/10.1175/BAMS-85-8-1095.

Weisman, M. L., and J. B. Klemp, 1986: Characteristics of isolated convective storms. *Mesoscale Meteorology and Forecasting*, P. S. Ray, Ed., Amer. Meteor. Soc., 331–358.

Wilks, D. S., 1995: *Statistical Methods in the Atmospheric Sciences: An Introduction.* International Geophysics Series, Vol. 59, Elsevier, 467 pp.

Wilson, M. B., and M. S. Van Den Broeke, 2021: An automated Python algorithm to quantify Z_{DR} arc and K_{DP}–Z_{DR} separation signatures in supercells. *J. Atmos. Oceanic Technol.*, **38**, 371–386, https://doi.org/10.1175/JTECH-D-20-0056.1.

Wurman, J., K. Kosiba, T. White, and P. Robinson, 2021: Supercell tornadoes are much stronger and wider than damage-based ratings indicate. *Proc. Natl. Acad. Sci. USA*, **118**, e2021535118, https://doi.org/10.1073/pnas.2021535118.

Zeitler, J. W., and M. J. Bunkers, 2005: Operational forecasting of supercell motion: Review and case studies using multiple datasets. *Natl. Wea. Dig.*, **29**, 81–97.

Ziegler, C. L., E. N. Rasmussen, T. R. Shepherd, A. I. Watson, and J. M. Straka, 2001: The evolution of low-level rotation in the 29 May 1994 Newcastle–Graham, Texas, storm complex during VORTEX. *Mon. Wea. Rev.*, **129**, 1339–1368, https://doi.org/10.1175/1520-0493(2001)129<1339:TEOLLR>2.0.CO;2.